Contents lists available at ScienceDirect

Journal of Sound and Vibration

journal homepage: www.elsevier.com/locate/jsvi

Three-dimensional effects of the wake on wind turbine sound propagation using parabolic equation

Hemant Bommidala [a], Jules Colas [a], Ariane Emmanuelli [a], Didier Dragna [a],*,
Codor Khodr [a], Benjamin Cotté [b], Richard J.A.M. Stevens [c]

[a] *Ecole Centrale de Lyon, CNRS, Université Claude Bernard Lyon 1, INSA Lyon, LMFA, UMR5509, 69130, Ecully, France*
[b] *IMSIA, ENSTA-CNRS-EDF, Institut Polytechnique de Paris, UMR9219, 91120, Palaiseau, France*
[c] *Physics of Fluids Group, Max Planck Center Twente for Complex Fluid Dynamics, J. M. Burgers Center for Fluid Dynamics, University of Twente, P.O. Box 217, 7500 AE Enschede, The Netherlands*

ARTICLE INFO

ABSTRACT

The influence of three-dimensional (3D) wind turbine wake effects on sound propagation is investigated. To study this, numerical simulations are conducted using a 3D parabolic equation model at low frequencies, with comparisons made to a two-dimensional (2D) approach that neglects transverse horizontal propagation. Three atmospheric stability conditions are investigated using analytical wind profiles that incorporate the wake effects. The wind turbine noise source is specified using an aeroacoustic extended source model. 3D effects due to the wake are shown to be significant, especially for the stable atmosphere. Indeed, horizontal refraction induces focusing that a 2D approach fails at predicting. As the wind turbine blades are rotating, the focal zones are moving accordingly, yielding large variations of the sound levels. Downstream the turbine, amplitude modulation can locally reach values as high as 16.5 dB over long distances. In addition, higher average SPL are predicted by 3D simulations compared to 2D ones, with deviations up to 4.5 dB. For neutral and unstable conditions differences in 2D and 3D sound propagation approaches are smaller, as velocity gradients in the wind turbine wake are smaller.

1. Introduction

While wind energy has a key role in the transition to sustainable energy, wind turbines have an impact on the environment. Noise annoyance for people living near wind farms is one of the obstacles to the growth of wind energy. It is partly due to sound pressure levels (SPL), although they remain small overall compared to other types of environmental noise, but also due to distinctive properties of wind turbine noise, such as amplitude modulation (AM) [1,2]. Compliance with noise regulations by wind farm operators is essential to mitigate neighborhood annoyance and to improve public acceptance. This makes the accurate prediction of noise levels and understanding of the underlying physical mechanisms critical.

Simulations of wind turbine noise propagation are challenging for two main reasons. Firstly, wind turbine noise is broadband, spanning frequencies up to several kilohertz. While a single-point source model at the rotor center suffices to calculate average sound pressure levels, it falls short in predicting amplitude modulation. Advanced models are based on multiple equivalent point sources to account for an extended and rotating source [3,4], but requires performing a much larger number of propagation simulations.

Secondly, the considerable distances over which wind turbine noise travels – sometimes audible several kilometers away [5,6] – add to the computational complexity.

As a consequence, three-dimensional (3D) simulations of wind turbine noise propagation are computationally demanding. Apart from geometrical acoustics [7,8], wave-based models typically use a two-dimensional (2D) approach. In these models, sound propagation is computed in a vertical plane containing the source and the receiver, neglecting any transverse propagation. The parabolic equation (PE) method is popular because of its efficiency and accuracy for long-range propagation (e.g., Lee et al. [9], Barlas et al. [3] and Kayser et al. [10]). We note that direct approaches using linearized Euler equations, which are better suited for complex terrains than PE, have also been developed [11,12].

Three-dimensional propagation effects are expected to be significant. They can be caused by topography or by the combined influence of the topography and the atmospheric boundary layer (ABL) dynamics. Wind veer, which is the change of wind direction with height, is also expected to yield 3D effects. Another source of 3D effects is the wake, that develops downstream of the wind turbine. Its impact on sound propagation has been first studied by Heimann et al. [13] using a 3D geometrical approach and flow profiles obtained from Reynolds-averaged Navier–Stokes equations. They found that the wake deficit acts as a duct carrying sound energy downstream. Barlas et al. [14] have further investigated the wake effect. They performed numerical simulations with a 2DPE approach using flow profiles obtained from either large-eddy simulations or from analytical models. They show that sufficiently far from the wind turbine, as the wake deficit reduces, the ducted sound waves impinge the ground, causing a large increase in SPL in the so-called downwards bursting zone. The study also investigated the sensitivity to ABL stability, showing that a stable atmosphere causes bursting zones closer to the wind turbine with the largest SPL increase. Later, Heimann and Englberger [7] investigate the diurnal variability of SPL downwind using a geometrical approach. In particular, they illustrate the importance of 3D effects. They indicate that 2D simulations neglect horizontal refraction and that 3D simulations are required to fully describe the effect of the wake on wind turbine noise propagation but no quantitative comparison between 2D and 3D results was made.

This study aims to address this gap by employing a 3D parabolic equation approach coupled with an extended noise source model to investigate the wake's impact on wind turbine noise propagation. For that, the case of a wind turbine above a flat and homogeneous ground is considered. Note that topography can have a significant impact on the wake shape and sound propagation, considerably enhancing and reducing the wake effect on wind turbine noise propagation [12]. In addition, for simplicity, scattering by atmospheric turbulence is not accounted for. This study represents the first 3D parabolic equation simulations conducted for wind turbine noise propagation. The objectives are threefold: (i) to present a comprehensive framework for 3D wind turbine noise propagation, (ii) to explore 3D effects induced by the wake in terms of sound pressure levels and amplitude modulation, and (iii) to quantify discrepancies with a 2D approach.

The paper is organized as follows. The scenario and the methods, including the wind turbine noise source model, the wind flow profile with a wake, and the propagation models are presented in Section 2. Three-dimensional effects due to the wake are discussed in Section 3 and are first illustrated based on a single point source. Using an extended source model, the case of a full wind turbine in a stable atmosphere is presented in Section 4. Section 5 extends the analysis to the neutral and unstable cases. Finally, concluding remarks are given in Section 6.

2. Methods

This section presents the considered scenario and details the sound propagation, noise source and flow models implemented in this study.

2.1. Scenario

A 3D Cartesian space is considered and is described by the coordinate system $\mathbf{x} = (x, y, z)$. A sketch of the problem is shown in Fig. 1(a). The domain of interest is $0 \leq x \leq 3000$ m, -300 m $\leq y \leq 300$ m, and $0 \leq z \leq 300$ m. The wind turbine rotor is located at the plane $x = 0$. The mean velocity in the ABL $\mathbf{U}$ is directed along the x-direction, i.e. $\mathbf{U} = (U_x, 0, 0)$. The ground at $z = 0$ is flat and absorbing. The wind turbine has a hub height $z_h = 90$ m and a rotor diameter $d_0 = 120$ m. The wind speed at hub height is set to $U_h = 11.4$ m/s. These parameters are based on the NREL 5MW turbine at rated wind speed [15]. The wind turbine blades rotate counterclockwise. In addition, the reference values for the sound pressure and sound power levels are 2×10^{-5} Pa and 1×10^{-12} W, respectively.

2.2. Atmospheric boundary layer and wind turbine wake model

For simplicity, we consider analytical flow profiles. The inflow wind profile U_∞ follows a power law [16]:

$$U_\infty = U_h \left(\frac{z}{z_h} \right)^\alpha \tag{1}$$

with α the power-law exponent that varies depending on the atmospheric stability. The temperature profile is constant, yielding a constant sound speed profile $c = c_0$, with $c_0 = 340$ m s^{-1}.

The wake formed in the downwind direction of the wind turbine plays an important role in the localization and formation of refraction patterns of the sound pressure fields. The analytical model developed by Bastankhah and Porté-Agel [17] is used for the
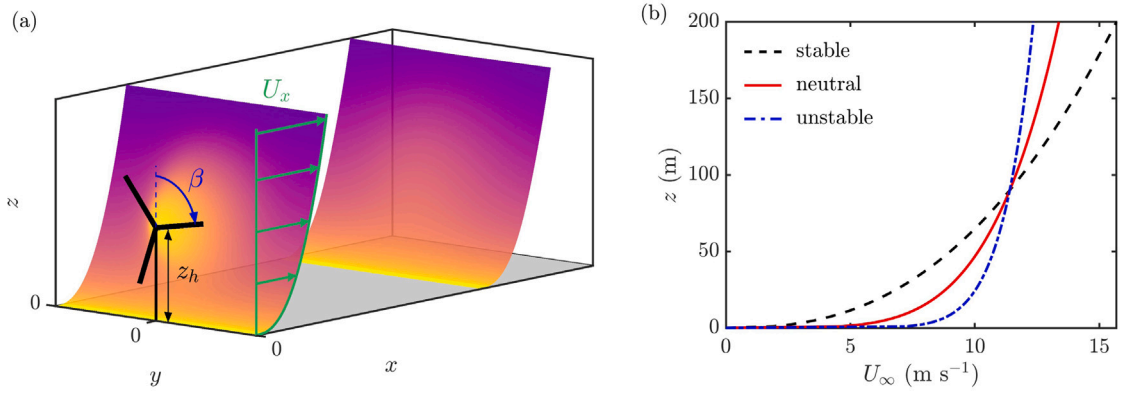
Fig. 1. (a) Sound propagation of wind turbine noise in the ABL. The surfaces representing the wind profiles at two different positions are colored by the velocity. (b) Inflow wind profiles for the (dashed) stable, (solid) neutral, and (dash-dotted) unstable atmosphere.

Table 1
Power-law exponent of the inflow wind profile α and wake growth rate k^* of the ABL flow for the three atmospheric conditions.

	Unstable	Neutral	Stable
α	0.1	0.2	0.4
k^*	0.05	0.03	0.02

wake velocity profile. It is obtained from the conservation equations of mass and momentum, assuming that the velocity deficit in the wind turbine wake has a Gaussian shape. The velocity deficit of the wake $\Delta U = U_\infty - U_x$ is defined as:

$$\frac{\Delta U}{U_\infty} = C(x) \exp\left(-\frac{y^2 + (z - z_h)^2}{2\sigma(x)^2}\right) \tag{2}$$

where $C(x)$ is the normalized velocity deficit along the wake centerline, given by:

$$C(x) = 1 - \sqrt{1 - \frac{C_T}{8}\left(\frac{d_0}{\sigma(x)}\right)^2} \tag{3}$$

with C_T the thrust coefficient of the wind turbine and σ the standard deviation, corresponding to the wake width. The analytical model assumes a linear expansion of the wake region, yielding:

$$\frac{\sigma(x)}{d_0} = k^* \frac{x}{d_0} + \kappa \tag{4}$$

with κ the value of σ/d_0 as x approaches zero, given by:

$$\kappa = \frac{1}{4\sqrt{2}}\left(1 + \frac{1}{\sqrt{1 - C_T}}\right)^{1/2}. \tag{5}$$

The thrust coefficient of the wind turbine C_T is set to 0.8 for all simulations, as in Barlas et al. [14]. Finally, $k^* = d\sigma/dx$ is the wake growth rate that depends on atmospheric stability.

The velocity profiles obtained with the Gaussian wake model by Bastankhah and Porté-Agel are in close agreement with measurements in the far wake ($x/d_0 > 4$). We note that, in the near wake, the Gaussian wake model predicts a velocity deficit that is too large and experiments show that the wake profile is not Gaussian. Refined models, such as the one by Blondel and Cathelain [18], have been proposed to correct these shortcomings at the expense of more intricate formulas. To highlight 3D effects, the Gaussian wake model has been deemed sufficient.

Three atmospheric conditions are considered, corresponding to an unstable, a neutral and a stable atmosphere. The values of α and k^* for each configuration are indicated in Table 1. They have been chosen according to the values reported in van der Berg [16] and in Abkar and Porté-Agel [19]. The inflow wind profiles for the three atmospheric stability conditions are presented in Fig. 1(b). 3D effects due to the wake are expected to be most significant for the stable case, as the wind speed gradient at hub height is the largest and as the wake growth rate is the smallest. The stable case serves as the reference configuration and is the primary focus of our discussion. The resulting ABL flow for a stable atmosphere is plotted in Fig. 2. The velocity deficit behind the wind turbine and the wake recovery are observable. Note that the maximum value of the normalized velocity deficit remains above 10% up to $x = 2500$ m for stable condition, but only up to $x = 1600$ m and 1000 m for neutral and unstable conditions, respectively.
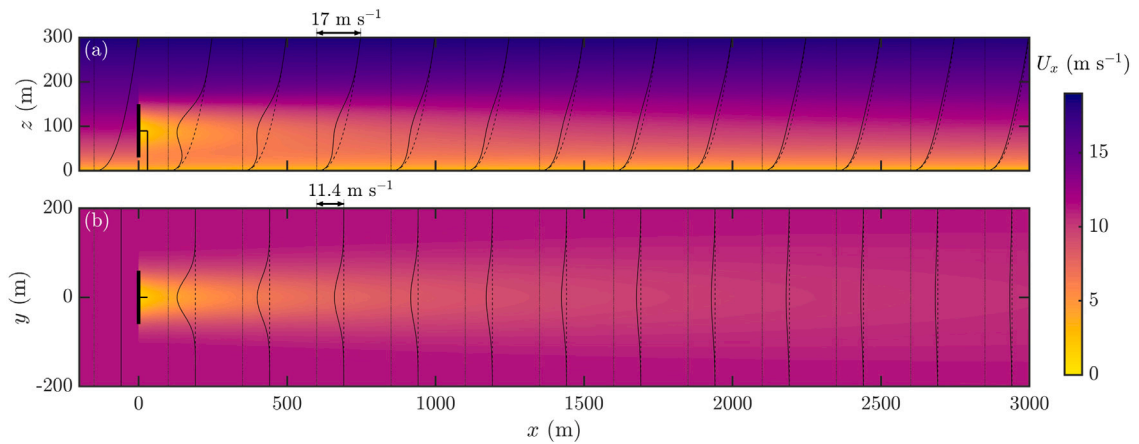
Fig. 2. Wind profiles for stable stratification on (a) the $x - z$ plane at $y = 0$ and (b) the x–y plane at $z = 90$ m corresponding to the hub height. The wind profiles are plotted at several positions as solid lines. The inflow wind profile is also plotted as dashed lines for reference.
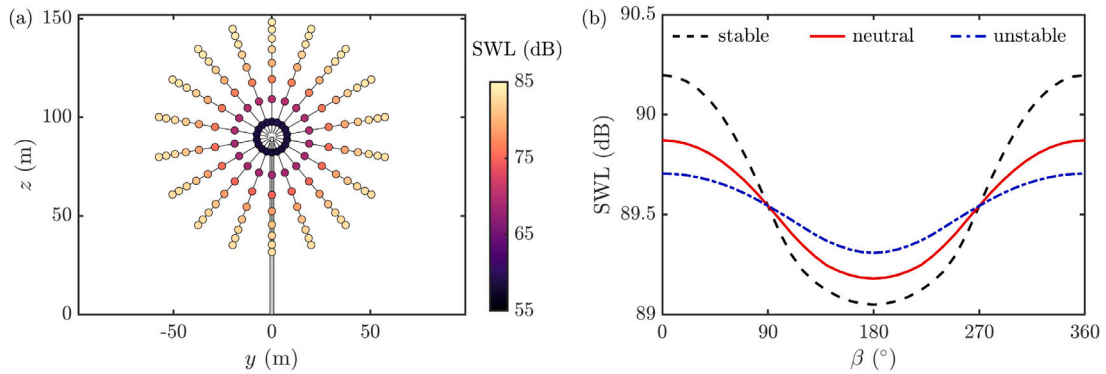
Fig. 3. (a) Location of the equivalent sources for the wind turbine and for a stable atmosphere. Each source is colored by its effective sound power level in free field. For readability, the angular step is set to 20° instead of 10°. (b) Sound power level for a single blade as a function of the blade angle β for the (dashed) stable, (solid) neutral, and (dash-dotted) unstable case. The frequency is 100 Hz for both figures.

2.3. Wind turbine noise source model

The study uses the wind turbine noise source model developed in Tian and Cotté [20], which focuses on aerodynamic noise. Mechanical noise is therefore omitted. The aerodynamic broadband noise from a large wind turbine in the audible range is essentially due to the unsteady forces induced by the turbulent flow on the blades. The noise source model is based on Amiet's theory for the prediction of turbulent inflow noise and trailing edge noise. As low frequencies are considered, turbulent inflow noise is the predominant noise source. In addition to the geometry of the blades, Amiet's theory requires several inputs: the inflow wind profile, the energy spectrum of the atmospheric turbulence for turbulent inflow noise, the spectrum of the wall pressure fluctuations near the trailing edge, and the corresponding spanwise correlation length for trailing edge noise. The Kolmogorov model is used for the energy spectrum of the atmospheric turbulence. It depends on a single parameter, the turbulent dissipation rate ϵ. Observations show that ϵ tends to decrease with height and depends on the stability condition (see, e.g., Han et al. [21]). For simplicity, this parameter is constant in this study and is set to $\epsilon = 0.01$ m^2 s^{-3} for the three atmospheric stability conditions. The spectrum of the wall fluctuating pressure on the blade surface is specified according to the Lee model [22], with boundary layer quantities evaluated using XFOIL [23]. Finally, the spanwise correlation length of the wall pressure fluctuations is prescribed using the Corcos model. In addition, blade rotation induces source motion effects, i.e. Doppler shift and convective amplification. This is accounted for in the source model by applying a frequency and amplitude correction following Sinayoko et al. [24].

The wind turbine corresponds to that employed in Tian and Cotté [20], except the rotor diameter is scaled up to 120 m instead of 93 m. Application of Amiet's theory to wind turbine noise requires to split the blades of the wind turbine into N_b independent segments. Each segment can then be represented by an equivalent point source located at the segment center, whose sound pressure level in free-field is given by Amiet's theory. We split each blade into $N_b = 8$ segments. The rotation of the blade is divided into 36 angular positions, corresponding to a resolution of 10°. The location of the equivalent sources in the rotor plane is shown in Fig. 3(a) (for readability, the angular resolution is 20°). Each source is colored by its effective sound power level downwind in free field

for a stable atmosphere and for a frequency of 100 Hz. The effective power has been determined by considering each equivalent source as a monopole: we can then relate in free-field the source power level SWL with the sound pressure level at an observer $\mathrm{SPL_{ff}}$ with the relation $\mathrm{SWL} = \mathrm{SPL_{ff}} + 10\log_{10}(4\pi R^2)$ where R is the distance between the segment center and the observer. It can be remarked that the three segments near the blade tip produce most of the noise. Fig. 3(b) represents the effective source power for a single blade as a function of the blade angle for a frequency of 100 Hz and for the three stability conditions. As the segments are independent, the source power has been obtained by adding the contributions of the N_b segments. For each stability case, the sound power level is maximal when the blade is pointing upwards ($\beta = 0°$), continuously decreases as the blade rotates, and reaches a minimum when the blade is pointing downwards ($\beta = 180°$). This is mostly due to the variation in wind velocity, as the sound power level is directly correlated to the wind velocity. The variation of the noise power production is largest for the stable case, reaching 1.2 dB.

2.4. Sound propagation models

Two propagation models are used to determine sound pressure levels in a 3D geometry. The first one, that is at the heart of the study, is a 3DPE model that fully describes 3D propagation effects. The second model is a $N \times 2$DPE model, which is the current state-of-the-art for the prediction of far-field wind turbine noise propagation [3].

2.4.1. 3DPE method

The 3D standard parabolic equation is solved to predict sound propagation in the ABL. It is an efficient approach for 3D long-range sound propagation. Indeed, as a one-way approach, the PE can be solved using a range-marching technique. From a starting field on a given plane, the solution is obtained on successive planes along a main propagation direction. This dramatically reduces the computational cost and the memory storage compared to a direct approach based on the linearized Euler equations, that requires a full-volume discretization. The main drawback of PE is the angular limitation: the PE is only accurate in a cone around the main propagation direction, whose angle is about 20° for the standard PE [25]. Formulations of PEs [26] with reduced phase errors have been recently proposed for moving media but have not been considered for this study. Here we use the 3DPE code developed by Khodr et al. [27]. It has been employed to study infrasound propagation over irregular terrain [28]. It is developed in curvilinear coordinates to account for topography; since this feature is not used in this study, the code is presented in Cartesian coordinates for simplicity.

The convention $\mathrm{e}^{-\mathrm{i}2\pi f t}$ is used throughout the paper. As sound propagation downwind of the wind turbine is considered, the main propagation direction is the x-direction. Introducing the complex pressure envelope ψ given by $p(\mathbf{x}, f) = \psi(\mathbf{x}, f)\,\mathrm{e}^{ik_0 x}$, the standard 3D parabolic equation reads as:

$$\frac{\partial \psi}{\partial x} = \frac{\mathrm{i}}{2k_0}\left(k_0^2 \epsilon_{\mathrm{eff}} + \frac{\partial^2}{\partial y^2} + \frac{\partial^2}{\partial z^2}\right)\psi \tag{6}$$

with $\epsilon_{\mathrm{eff}} = (c_0/c_{\mathrm{eff}})^2 - 1$, $k_0 = 2\pi f/c_0$ and c_0 the reference sound speed. Finally, the parameter $c_{\mathrm{eff}}(\mathbf{x}) = c + U_x(\mathbf{x})$ is the effective sound speed. The main elements of the PE solver are as follows. The Crank–Nicolson marching scheme is used in the x-direction and the second order derivatives are discretized with second-order finite-differences in the transverse plane. The resulting set of equations is recast into a matrix equation that involves the inversion of tridiagonal matrices. It is solved using an efficient iterative fixed-point method.

The simulations are initialized at plane $x = 0$ with a Gaussian starter representing a monopole source located at $\mathbf{x}_S = (0, y_S, z_S)$:

$$\psi(x = 0, y, z) = ik_0 S_0 \exp\left(-\frac{k_0^2[(y - y_S)^2 + (z - z_S)^2]}{2}\right) \tag{7}$$

with $S_0 = 1$ Pa m. An impedance boundary condition is set at the ground surface. The ground surface impedance is prescribed using Attenborough's four parameter model [29]. To represent grassy ground, we use a flow resistivity of 200 kPa s m^{-2}, a porosity of 0.3, a grain shape factor of 0.5, and a pore shape factor ratio of 0.75. Absorbing layers are used at the outer boundaries to simulate an unbounded domain in such a way that the waves are gradually attenuated in the absorbing layers avoiding unwanted reflections into the computational domain. In accordance with the guidelines given in Salomons [30], a safe value of 100 wavelengths is chosen for the thickness of the absorbing layers. Finally, the output of the PE simulation is the sound pressure level relative to the free field ΔL, calculated with:

$$\Delta L(\mathbf{x}, \mathbf{x}_S, f) = 20\log_{10}\left(\frac{|p(\mathbf{x}, f)|R}{S_0}\right) \tag{8}$$

with $R = |\mathbf{x} - \mathbf{x}_S|$ the source–receiver distance.

2.4.2. $N \times 2$DPE method

The current state-of-art for wind turbine sound propagation is the 2DPE method [3,9,10]. Results can be obtained in a 3D geometry by performing multiple simulations in vertical slices around the source. This method is known as the $N \times 2$DPE method (see, e.g., Sturm [31]). As 2D simulations are performed, out-of-plane propagation is neglected. While this approach is suitable if the wind and temperature profiles depend only on the vertical coordinate, it may be inaccurate otherwise since it does not account for horizontal refraction.

Table 2

Configurations investigated in this study, with both 3DPE and $N \times 2$DPE methods. The abbreviations "ABL" and "ABL+wake" indicate the flow used consists of respectively the ABL profile only (no wake) and a profile that includes the wake.

Frequency (Hz)	50	75	100	125
Stable	ABL+wake	ABL+wake	ABL, ABL+wake	ABL+wake
Neutral			ABL, ABL+wake	
Unstable			ABL, ABL+wake	

For consistency with the 3DPE method, we consider the 2D narrow-angle PE. The 2DPE is solved in a vertical $r - z$ plane, with r the horizontal distance to the source ($x = r\cos\theta$, $y = y_S + r\sin\theta$) and θ the azimuthal angle. Introducing the 2D pressure envelope ϕ related to the acoustic pressure by $p(\mathbf{x}, f) = \phi(r, z, f)\mathrm{e}^{\mathrm{i}k_0 r}/\sqrt{r}$, the standard 2D parabolic equation reads:

$$\frac{\partial \phi}{\partial r} = \frac{\mathrm{i}}{2k_0}\left(k_0^2 \epsilon_{\mathrm{eff}} + \frac{\partial^2}{\partial z^2}\right)\phi \tag{9}$$

Note that, even if 2D simulations are performed, the pressure decay with distance follows the spherical spreading law due to the definition of the pressure envelope. In the 2DPE approach, the effective sound speed accounts for the horizontal component of the wind speed in the vertical plane. This writes $c_{\mathrm{eff}}(r, z) = c + U_x(r\cos\theta, y_S + r\sin\theta, z)\cos\theta$.

As for the 3DPE, the simulations are initialized at $r = 0$ with a Gaussian starter to represent a monopole source:

$$\phi(r = 0, z) = \sqrt{\mathrm{i}k_0}\, S_0 \exp\left(-\frac{k_0^2(z - z_S)^2}{2}\right). \tag{10}$$

An impedance boundary condition is set at the ground surface, with the same impedance model and parameters as in the 3DPE. A perfectly matched layer is used at the top boundary as a non-reflecting boundary condition. The relative sound pressure level is calculated similarly to 3DPE using Eq. (8).

2.5. Linking between noise source model and propagation model

The wind turbine source model discussed in Section 2.3 allows one to predict sound pressure levels in the free-field, which is denoted as $\mathrm{SPL}_{\mathrm{ff}}$. Atmospheric and ground effects are accounted for by the propagation model described in Section 2.4. The linking between the source and propagation models is described below.

Following Cotté [4], the sound pressure level at a receiver $\mathbf{x}$ due to the segment m of the blade for an angular position β located at $\mathbf{x}_S(\beta, m)$ is calculated with:

$$\mathrm{SPL}(\mathbf{x}, f, \beta, m) = \mathrm{SPL}_{\mathrm{ff}}(\mathbf{x}, f, \beta, m) + \Delta L(\mathbf{x}, f, \beta, m) - \mu(f)R \tag{11}$$

where μ is the atmospheric absorption coefficient and ΔL is the sound pressure relative to the free-field determined with a propagation model. Since we limit our study to low frequencies, the effects of atmospheric absorption are small: for a frequency of 100 Hz, reduction of noise levels is below 1 dB for propagation distances up to 3 km. Consequently, we neglect atmospheric absorption in what follows, i.e $\mu \approx 0$. As blade segments are modeled as incoherent sources, the SPL due to a single blade at a given angular position β is then obtained by summing the contributions from all segments:

$$\mathrm{SPL}(\mathbf{x}, f, \beta) = 10\log_{10}\left(\sum_{m=1}^{N_b} 10^{\mathrm{SPL}(\mathbf{x}, f, \beta, m)/10}\right). \tag{12}$$

Finally, we obtain the SPL for the full wind turbine, noted as $\mathrm{SPL}_T(\mathbf{x}, f, \beta_T)$, by adding the contributions from the three blades at $\beta = \beta_T$, $\beta = \beta_T + 2\pi/3$, and $\beta = \beta_T + 4\pi/3$.

To quantify average noise levels, we use the SPL averaged over one rotation, denoted by $\overline{\mathrm{SPL}_T}$ and calculated with:

$$\overline{\mathrm{SPL}_T}(\mathbf{x}, f) = 10\log_{10}\left(\frac{3}{2\pi}\int_0^{2\pi/3} 10^{\mathrm{SPL}_T(\mathbf{x}, f, \beta_T)/10}\,\mathrm{d}\beta_T\right). \tag{13}$$

Amplitude modulation of the SPL plays an important role in characterizing wind turbine annoyance (see, e.g., Lee et al. [1]). We define AM as the difference between the maximum and minimum SPL during one rotation:

$$\mathrm{AM}(\mathbf{x}, f) = \max_{\beta_T}[\mathrm{SPL}_T(\mathbf{x}, f, \beta_T)] - \min_{\beta_T}[\mathrm{SPL}_T(\mathbf{x}, f, \beta_T)]. \tag{14}$$

2.6. Numerical parameters

Simulations are performed for the three atmospheric stability conditions presented in Section 2.2 and for four frequencies, $f = 50$, 75, 100 and 125 Hz. They have been carried out using wind profiles consisting of either the ABL profile or a profile that includes the wake. The configurations investigated in the paper are indicated in Table 2. Since each wind turbine blade is split into 8 segments

Table 3
Mesh size and computational time for different frequencies required for 3DPE method.

Frequency (Hz)	50	75	100	125
Mesh size	1.7×10^9	5.8×10^9	1.4×10^{10}	2.7×10^{10}
Computational time (CPU h)	1.5×10^3	4.5×10^3	9.1×10^3	2.1×10^4
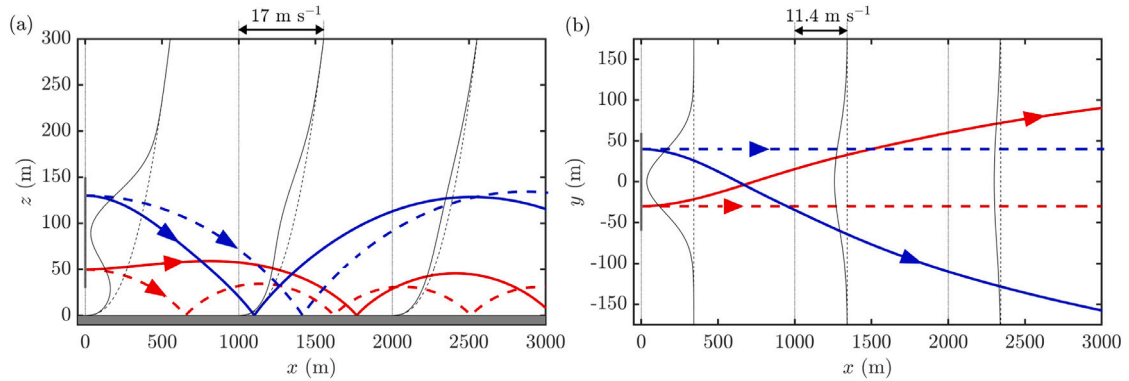
Fig. 4. Trajectories of two rays launched from the rotor are indicated in thick lines: solid lines account for the turbine wake, while dashed lines do not. Projections are displayed in (a) the $x - z$ plane at $y = 0$ and (b) the x–y plane at $z = 90$ m corresponding to the hub height. The superimposed velocity profiles in gray represent the velocity profile in the ABL, with solid lines including the turbine wake and dashed lines excluding it.

and the angular resolution is 10°, the total number of source positions is equal to 288. As the plane $y = 0$ is a plane of symmetry for the problem, the number of unique source positions for which propagation simulations are performed is reduced to 152.

For the 3DPE, the mesh grid is uniform and the grid steps are set to $\Delta x = \Delta y = \Delta z = \lambda/10$, with the wavelength $\lambda = c_0/f$. For the largest frequency of interest ($f = 125$ Hz), there are about 2.4×10^6 grid points in the plane $y - z$ and the number of spatial iterations along the x-direction is 1.1×10^4; this yields approximately a computational domain of 2.7×10^{10} points. This figure highlights the large number of degrees of freedom required by 3D wave-based methods for long range sound propagation, even at low frequencies. Details on the mesh size and total CPU time are given in Table 3.

For the $N \times 2$DPE, the planes around the z-axis are discretized using a uniform mesh with grid steps equal to $\lambda/10$. Results on horizontal and vertical planes are obtained using interpolation. The computational cost for $N \times 2$DPE method is significantly lower compared to the 3DPE method, with the CPU time amounting to just a few hours on a laptop.

3. 3D propagation effects due to the wake

3.1. Geometrical analysis of 3D propagation effects

The presence of the wake strongly affects the propagation of sound waves generated by the wind turbine. Insights on the effect of the wake on sound propagation can be gained from geometrical acoustics. The results shown thereafter have been obtained in stable conditions using a ray-tracing code based on Scott et al. [32].

3.1.1. Refraction
The wake corresponds to a velocity deficit and acts as a waveguide that carries sound energy downwind. As the velocity deficit gradually reduces with distance to the turbine, the waveguide effect induced by the wake becomes less efficient. At a certain distance, sound energy escapes from the wake and reaches the ground, significantly increasing sound levels in a region referred to as the 'downwards bursting zone' by Barlas et al. [14].

To illustrate the effect of the wake on sound propagation, we plot in Fig. 4 the trajectory of two rays launched from the rotor at two different positions with direction normal to the rotor plane. The projection of the trajectory onto the $x - z$ plane is plotted in Fig. 4(a). Concerning the ray initially located above the hub, the wind speed gradient at its initial position is positive and it has a stronger amplitude in the presence of the wake than without it. Therefore, compared to the case without the wake, the ray is refracted downwards more rapidly and then follows a similar trajectory. For the ray initially located below the hub, the wind speed gradient is negative due to the wake. As a consequence, the ray propagates upwards into the wake and gets deflected downwards when the wake disappears. Without the wake, the velocity gradient is positive at the initial location, and the ray is directly refracted downwards. Fig. 4(b) shows the projection of the ray trajectories onto the x–y plane. First, note that the rays without the wake do not suffer any refraction in the horizontal direction and their trajectory in a horizontal plane is a straight line. On the other hand, the wake induces large deviations of the rays. Thus, the ray initially located in the half-space $y > 0$ is found at $y < 0$ for $x > 630$ m. Conversely, the ray initially located in the half-space $y < 0$ is found at $y > 0$ for $x > 730$ m.
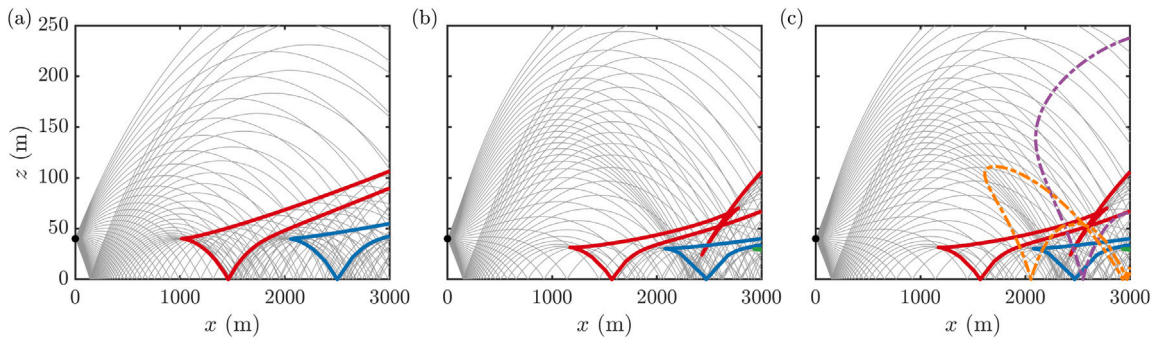
Fig. 5. Rays in thin gray lines originating from a source at $y_S = 0$ and $z_S = 40$ m and launched in the plane $y = 0$ with caustics in thick lines: (a) ignoring the wake, (b) accounting for the wake and ignoring horizontal refraction, and (c) accounting for the wake and horizontal refraction.
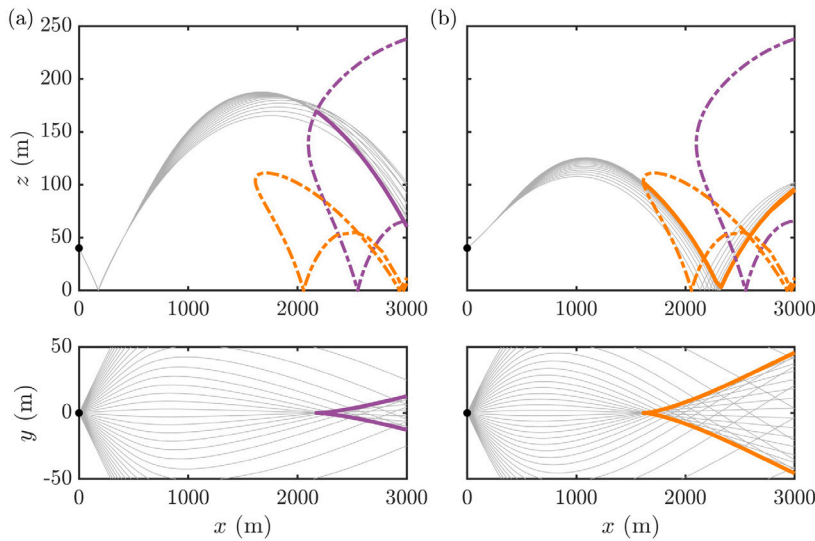
Fig. 6. Rays originating from a source at $y_S = 0$ and $z_S = 40$ m launched with an elevation angle set to (a) $-12°$ and (b) $5°$. The top and the bottom figures show the projection of the ray trajectories in the $x - z$ and $x-y$ planes, respectively. The thick solid lines represent the caustics associated with the rays and the thick dash-dotted lines are the caustic curves determined in the plane $y = 0$ shown in Fig. 5.

3.1.2. Focusing and caustics

Caustics are particular surfaces along which the ray-tube area is zero. In the high-frequency approximation, sound pressure amplitude is theoretically infinite along caustics. In reality, the sound pressure is finite but significantly elevated along these surfaces. Caustics indicate the regions where significant focusing of sound is expected.

A downward-refracting atmosphere generates near-ground caustics, whose structure is modified by the wake. Fig. 5 exemplifies the effect of the wake on the caustics for a source located at $y_S = 0$ and $z_S = 40$ m. Rays and caustics have been determined in the plane $y = 0$ for an azimuthal launch angle set to zero and elevation launch angles between -15 and $15°$. In Fig. 5(a), the rays and caustics are plotted for an atmosphere without the wake. The caustic structure is classical for a downward-refracting atmosphere (see, e.g. [30]). We observe two caustic curves, plotted by thick solid lines. Fig. 5(b) shows the rays and caustics considering the wake but without horizontal refraction. For that, we have neglected all the terms related to the transverse derivative of the mean flow in the ray equations. The caustics are modified by the presence of the wake. Note the focusing of the rays traveling downwards and hitting the ground around $x = 2200$ m. The caustic observed for $x > 1000$ m is significantly altered after reflection of these focused rays due to the wake. Finally, we represent in Fig. 5(c) the rays and caustics obtained by solving the full ray equations, which thus takes into account horizontal refraction within the wake. Compared to Fig. 5(b), the same rays are obtained. However, horizontal refraction modifies the ray-tube area along the rays, which, in turn, changes the caustic structure. Therefore, while the caustics in thick solid lines are exactly the same as in Fig. 5(b), two additional caustics in thick dash-dotted lines can be observed.

In order to understand the origin of these additional caustics, we plot in Fig. 6 the ray trajectories for the same source and for two elevation launch angles and for azimuthal launch angles between -10 and $10°$. Fig. 6(a) considers rays with an initial elevation angle of $-12°$. During propagation, the rays continuously undergo horizontal refraction due to the wake. After reflection from the ground, this generates a caustic curve starting from $x = 2100$ m. It corresponds to one of the two caustics appearing in
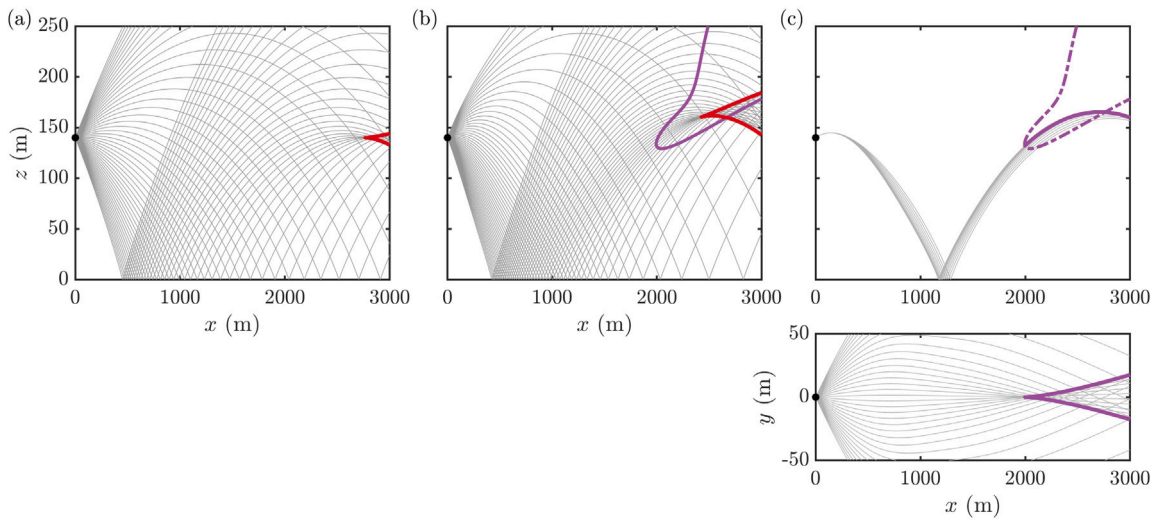
Fig. 7. Rays in thin gray lines originating from a source at $y_S = 0$ and $z_S = 140$ m and caustics in thick lines. The rays are launched in the plane $y = 0$ (a) ignoring the wake and (b) accounting for the wake. In (c), the rays are launched accounting for the wake with an elevation angle of 4° and for several azimuthal angles. The caustic in dash-dotted line corresponds to that determined in the plane $y = 0$ shown in (b).

thick dash-dotted lines in Fig. 5(c) and looks like a cusp in the x–y plane. In Fig. 6(b), the trajectories of rays launched with an elevation angle of 5° are plotted. Here again, horizontal refraction induces a caustic for $x > 1700$ m, which corresponds to the other caustic appearing in Fig. 5(c). Note that this caustic first originates from rays that have not been reflected on the ground and that is why it appears closer to the source.

The caustics change with the source position. As an illustration, Fig. 7 presents the rays and caustics for a source at $y_S = 0$ and $z_S = 140$ m. In Fig. 7(a) and (b), the rays are launched in the plane $y = 0$ for a wind profile with or without the wake. Without the wake, a single caustic curve is identified. It appears at a longer distance than in Fig. 5(a) because the source is located at a higher height. However, a similar caustic pattern as in Fig. 5(a) is expected. With the wake, Fig. 7(b) shows the focusing of the rays with a focus at $x = 2450$ m and $z = 160$ m. The caustic curve noticed in Fig. 7(a) is modified by the presence of the wake. In addition, a second caustic curve is observed. The trajectories of rays launched with an elevation angle of 4° and with azimuthal angles between −10 and 10° are plotted in Fig. 7(c). It is concluded that this additional caustic is again due to horizontal refraction.

3.2. Illustration of 3D effects for a single source with PE simulations

3.2.1. Focusing

We first illustrate the difference in the focusing zones predicted by $N \times 2$DPE and 3DPE. As for all the simulations in this section, the source frequency is 100 Hz. Fig. 8 presents the relative sound pressure levels ΔL for a source located at $y_S = 0$ and three different heights, corresponding to the hub height and to the hub height plus or minus 80% of the blade length ($z_S = 40$ and 140 m). They have been determined using 3DPE for the ABL without the wake and using 3DPE and $N \times 2$DPE for the ABL with the wake. We have checked that 3DPE and $N \times 2$DPE yield similar results without the wake. In what follows, the level maps obtained without the wake are determined with 3DPE. Also, we display the results only for $x > 500$ m, because the narrow-angle PE is not valid in the near-field. Without the wake in Fig. 8(a), (b), and (c), the maps of ΔL show downward refraction due to the power-law wind profile. As expected, the levels do not depend on y. Note the strong constructive and interference patterns on the ground for the source located below the hub in Fig. 8(c).

With the wake, the contour maps for the 3DPE highlight the focusing due to the velocity deficit behind the turbine. The focusing region appears in the plane $y = 0$ as a beam, that is first refracted downwards from the source, then hits the ground and is refracted downwards again. The focusing strongly depends on the source height. Its footprint on the plane $z = 0$ is observed close to the source for $z_S = 140$ m in Fig. 8(d), and moves away as the source height is reduced. In the plane $x = 3000$ m, we observe a large increase in the levels along a horizontal line, especially for $z_S = 140$ m. It is due to the inflow wind profile and is also seen without the wake in Fig. 8(a). We also observe an increase in SPL along the vertical line $y = 0$. In particular, note the round spot with the largest levels at the intersection between the focusing beam and the plane $x = 3000$ m. Its location also varies with source height.

Comparing the results for 3DPE and $N \times 2$DPE, it is clear that the $N \times 2$DPE approach captures most of the propagation effects due to the wake. Thus, the interference patterns on the planes $z = 0$ or $x = 3000$ m appear at the same locations for both approaches, as observed in Fig. 8 (f) and (i). Outside of the focusing region, the levels with $N \times 2$DPE are in close agreement with those of 3DPE. Also, the presence and the location of focusing is accurately predicted using $N \times 2$DPE. However, because horizontal refraction is neglected, $N \times 2$DPE underestimates the levels in the plane $y = 0$. In particular, the round spot in plane $x = 3000$ m, which exhibits the highest levels in the 3DPE, is absent in the $N \times 2$DPE.
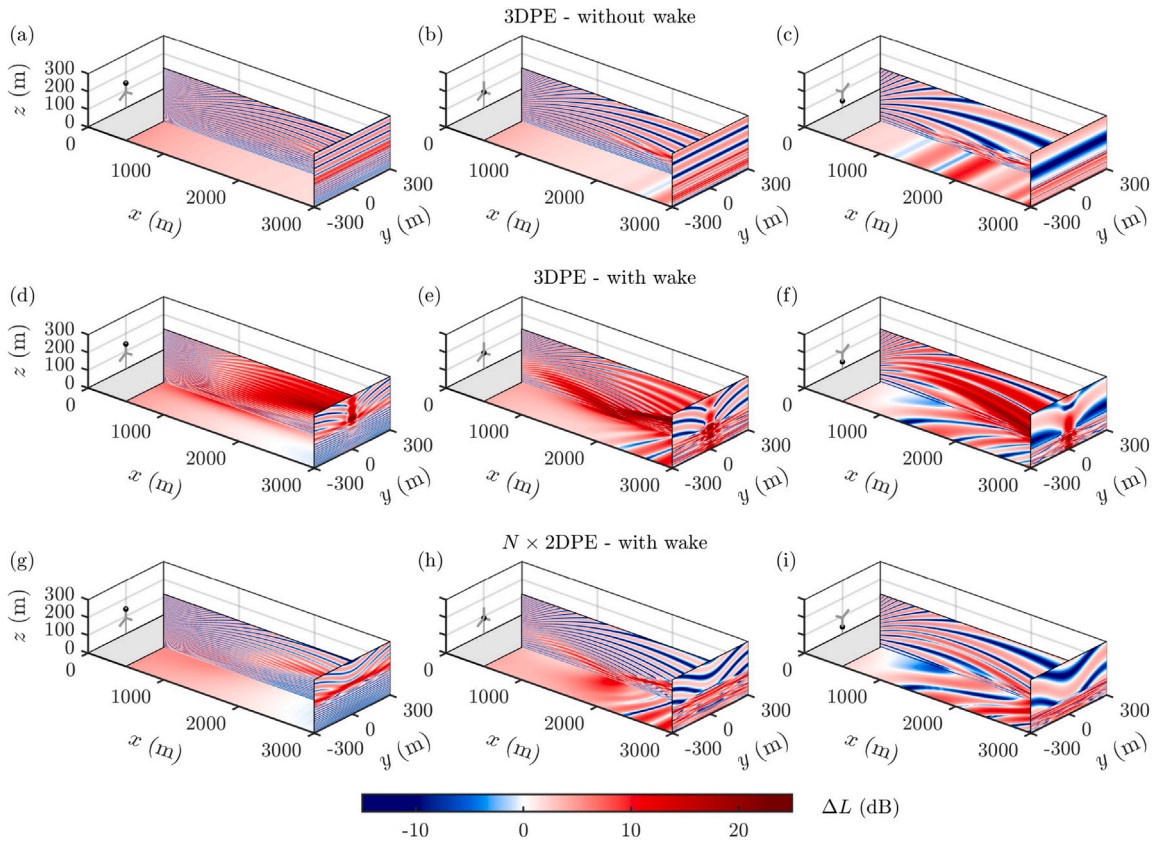
Fig. 8. Sound pressure levels relative to the free-field ΔL in the planes $x = 3000$ m, $y = 0$, and $z = 0$ for a source located at $y_S = 0$ and at three different heights computed with (a)–(c) 3DPE without wake, (d)–(f) 3DPE with wake and (g)–(i) $N \times$2DPE with wake. The source height is $z_S = 140$ m in (a), (d), and (g), $z_S = z_h$ in (b), (e), and (h), and $z_S = 40$ m in (c), (f), and (i). The source is indicated by a black dot.
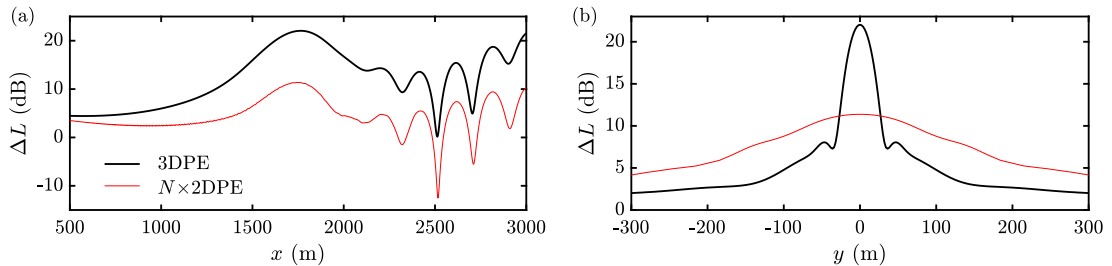
Fig. 9. Sound pressure levels relative to the free-field ΔL for a source located at the hub along the line (a) $y = 0$ and $z = 0$ and (b) $x = 1700$ m and $z = 0$ and for the two propagation models (thick lines) 3DPE and (thin lines) $N \times 2$D PE.

    To quantify the difference in sound pressure levels, Fig. 9 compares the relative levels for the two approaches for a source located at the hub. The evolution of ΔL along the line $y = 0$ and $z = 0$ is plotted in Fig. 9(a). For 3DPE, one notes a bump with a large increase centered at $x = 1700$ m, corresponding to the downwards bursting zone observed in Fig. 8(e) and followed by an interference pattern for $x > 2200$ m. The results for the $N \times 2$DPE show a similar evolution, but the levels are systematically lower, by 10 dB for $x > 1700$ m. Fig. 9(b) shows the evolution of ΔL along the line $x = 1700$ m and $z = 0$. For 3DPE, the zone in which ΔL is large is restricted to a narrow region with a width of about 70 m below the wind turbine wake. Outside this zone the levels rapidly decrease and are almost constant for $|y| > 100$ m. For $N \times 2$DPE, the peak ΔL at $y = 0$ is much lower than with 3DPE. Its reduction in the y-direction is also smoother, leading to ΔL levels about 2 dB larger with $N \times 2$DPE outside of the 3DPE peak.

3.2.2. Out-of-plane propagation
    We now exemplify the effect of out-of plane propagation on the pressure fields. For that, we consider a source at the hub height and with three different positions along the y-axis, corresponding to different positions along the blade. Fig. 10 shows the relative
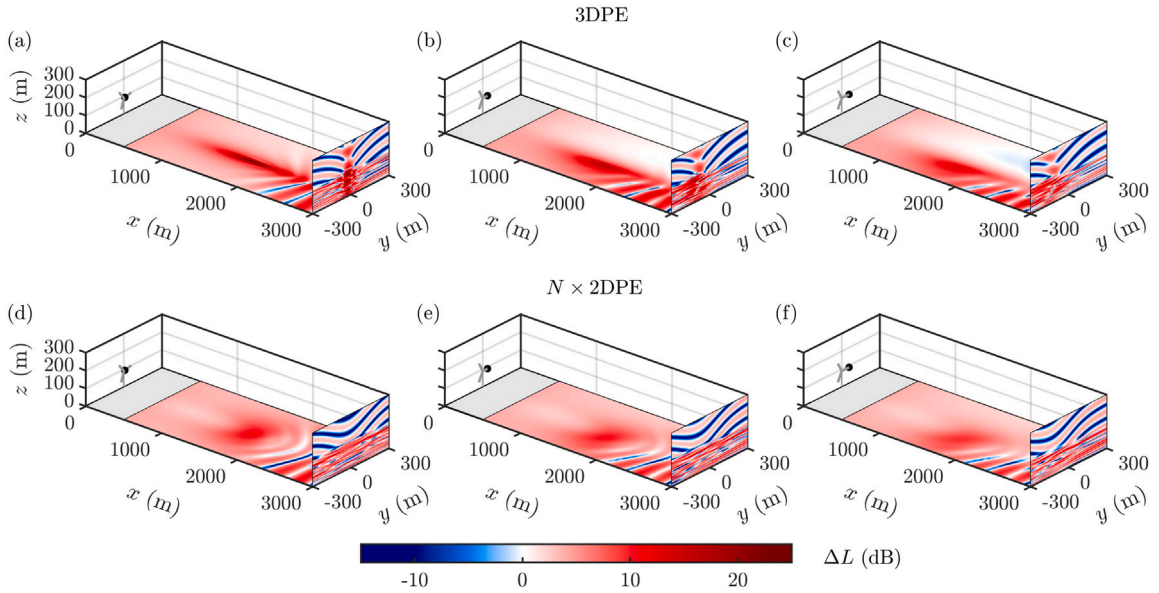
Fig. 10. Sound pressure levels relative to the free-field ΔL in the planes $x = 3000$ m and $z = 0$ for a source located at hub height and at several positions along the y-axis computed with (a)–(c) 3DPE and (d)–(f) $N \times 2$DPE. The source is located at $y_S = 7.8$ m in (a) and (d), $y_S = 37.6$ m in (b) and (e), and $y_S = 58.3$ m in (c) and (f). The source is indicated by a black dot.
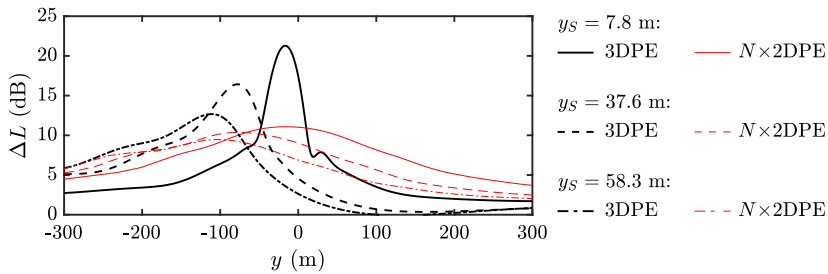
Fig. 11. Sound pressure levels relative to the free-field ΔL along the line $x = 1700$ m and $z = 0$ for a source located at the hub height and at (solid) $y_S = 7.8$ m, (dashed) $y_S = 37.6$ m, and (dash-dotted) $y_S = 58.3$ m, and for two propagation models: (thick lines) 3DPE and (thin lines) $N \times 2$DPE.

levels computed with the 3D and $N \times 2$DPE approaches. The former is used in Fig. 10(a), for which the source is located close to the hub. As in Fig. 8(e), a large focusing region can be observed along the line $y = 0$ for x between 1000 and 2000 m in the plane $z = 0$. Additionally, there is an increase in ΔL along the vertical axis for $y = 0$ in the plane $x = 3000$ m. As the source is moved towards the blade tip in Fig. 10 (b) and (c), the footprint of the focusing region in the plane $z = 0$ is shifted along the y-axis in the opposite direction. The maximum of ΔL reduces concurrently. In addition, the vertical line of increased levels in the plane $x = 3000$ m is progressively tilted counterclockwise. The round spot also shifts towards $y < 0$ and appears more and more blurred as y_S increases. In agreement with 3DPE, the results for $N \times 2$DPE show the presence of the focal zone on the plane $z = 0$ for the three source positions and its displacement towards the halfplane $y < 0$, as y_S increases. However, the focal zone is more spread out in the $N \times 2$DPE results and the maximum of ΔL has a smaller value. Finally, note the close correspondence between 3DPE and $N \times 2$DPE results in the interference pattern on the plane $x = 3000$ m for the three source positions. However, as indicated previously, the vertical line of increased levels in this plane is not predicted by $N \times 2$DPE as it neglects horizontal refraction and therefore fails to predict the corresponding caustics.

Fig. 11 shows the variations of ΔL along the line $x = 1700$ m and $z = 0$ for the three source locations along the blade considered in Fig. 10 for 3DPE and $N \times 2$DPE. We selected $x = 1700$ m because the highest sound levels are recorded there. The curves of ΔL obtained with the 3DPE present a peak, which broadens as y_S increases and whose maximum value decreases with increasing y_S. $N \times 2$DPE accurately predicts the location of the peak but underestimates the peak level by more than 10 dB for $y_S = 7.8$ m but only by 3 dB for $y_S = 58.3$ m.
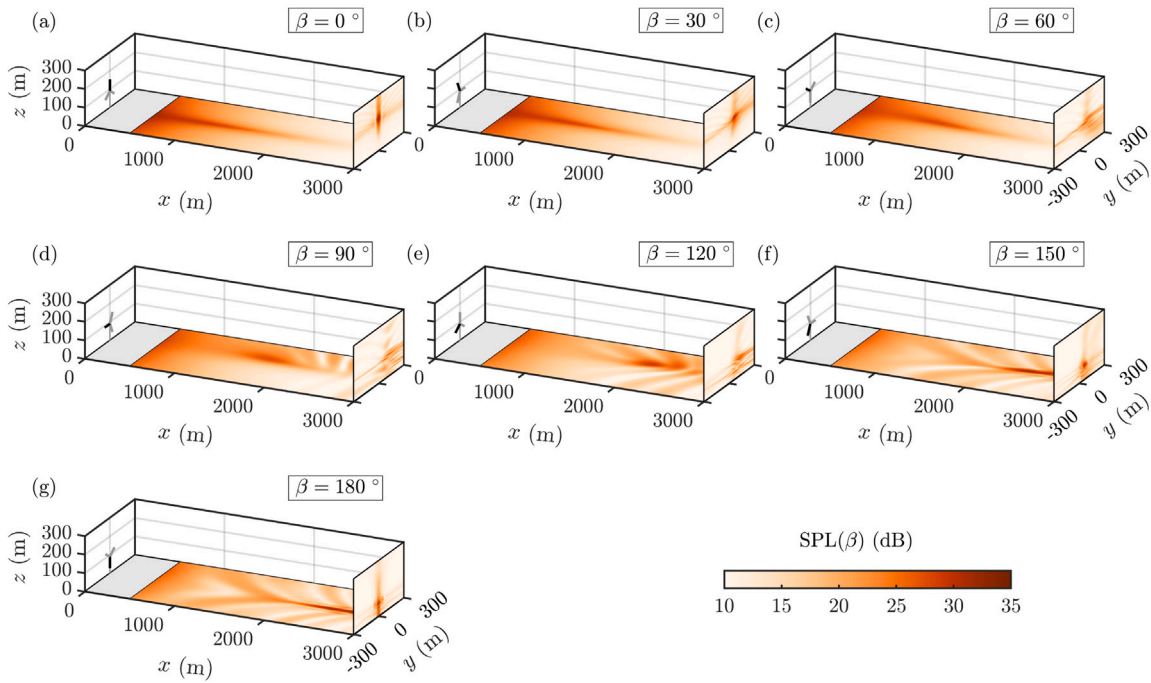
Fig. 12. Sound pressure levels SPL(β) in the planes $x = 3000$ m and $z = 0$ computed with 3DPE due to a single wind turbine blade and for seven angular positions: (a) $\beta = 0°$, (b) 30°, (c) 60°, (d) 90°, (e) 120°, (f) 150°, and (g) 180°. The blade emitting sound is colored in black.

4. Wind turbine noise propagation in a stable boundary layer

Sound pressure fields for the wind turbine are now examined. In this section, the analysis is carried out for a stable atmosphere and for a source frequency of 100 Hz. The corresponding results for different frequencies are reported in Appendix A.

4.1. Instantaneous fields depending on the blade and rotor orientation

Before considering the full wind turbine, we first examine the results for a single blade. Fig. 12 shows the sound levels for seven angular positions of the blade. As a reminder, the levels are obtained by adding the contributions of all segments of the blade. Overall, the levels are small – between 10 and 20 dB –, except near focal zones for which the levels can reach up to 32 dB. The focal zones are observed at different positions depending on blade orientation. Thus, on the plane $z = 0$, the focal zone is close to the source and up to $x \approx 2000$ m along the line $y = 0$ when the blade points upwards ($\beta = 0°$). As the blade rotates counterclockwise, the focal zone moves away from the wind turbine along the x-axis. Also, it first shifts towards $y > 0$ before returning towards $y = 0$ for $\beta > 90°$. Finally, when the blade is pointing downwards ($\beta = 180°$), the focal zone appears along the line $y = 0$ again, but for $x > 2000$ m. On the plane $x = 3000$ m, there are at least three zones with increased levels. The first focal zone is due to the underlying wind profile and would be present without wake. It corresponds to a horizontal line, that moves down as the blade is rotating. It is mostly observed when the blade is above the hub, i.e. for $\beta < 90°$, and it increases in intensity with source height. The two other focal zones are due to the wake. A distinct focal zone can be noticed along the vertical line $y = 0$ when the blade points upwards or downwards ($\beta = 0°$ or 180°). Note especially the round spot with large levels, which was already highlighted in Fig. 8 for a point source. The last focal zone is observed for $y > 0$ when the angular position of the blade is 90°. Note again that the largest levels are obtained in the half-plane opposite to the one containing the sources because of horizontal refraction. (An animation showing the SPL as the blade is rotating with and without wake and computed with 3DPE and $N \times$ 2DPE is provided as supplementary material (movie 1).)

These observations are in agreement with results for wind turbine sound propagation over a smooth hill by Heimann et al. [8]. They showed an increase in SPL for 200 m $< x <$ 1000 m when the source is above hub height and a corresponding decrease of SPL when the source is below hub height. Also, one can recognize from Fig. 7 in Heimann et al. [8] the effect of horizontal refraction, with increased levels at long range for $y < 0$ when the source is located at $y > 0$, and vice versa.

Now, the results for the full wind turbine are presented. The maps of SPL are shown in Fig. 13 for four angular positions of the blades. The sound levels are obtained by adding the contributions of the three blades. For each value of β_T, three zones with large SPL are noticed in the planes $z = 0$ and $x = 3000$ m. Each of these zones is due to one of the blades and can be identified using Fig. 12. Thus, for $\beta_T = 0°$, the focal zone in the plane $z = 0$ observed along $y = 0$ and for $x < 1700$ m is due to the upwards pointing
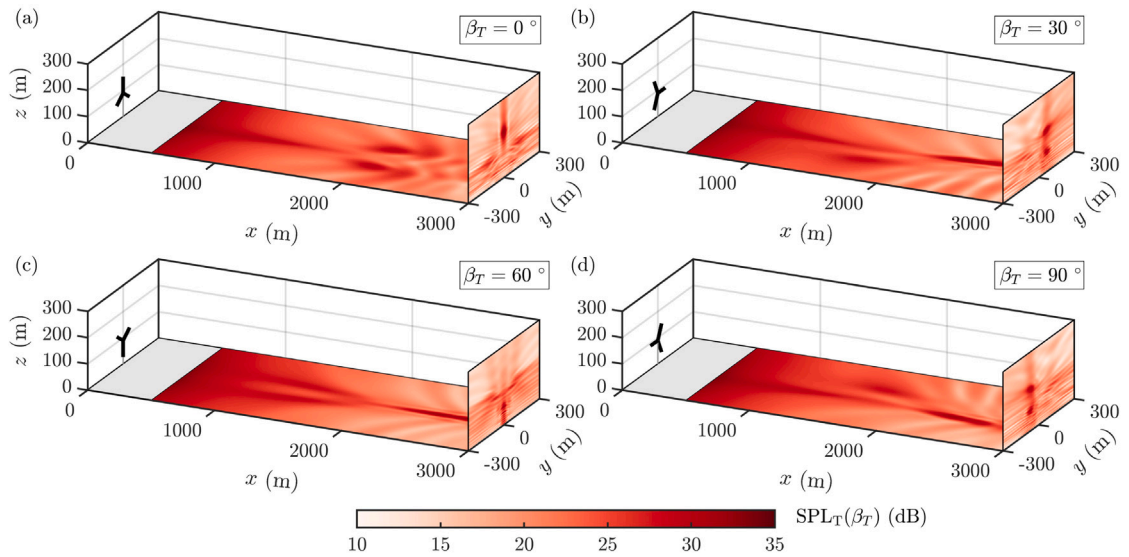
Fig. 13. Sound pressure levels $SPL_T(\beta_T)$ in the planes $x = 3000$ m and $z = 0$ computed with 3DPE for the full wind turbine and for four angular positions: (a) $\beta_T = 0°$, (b) 30 °, (c) 60 °, and (d) 90 °.
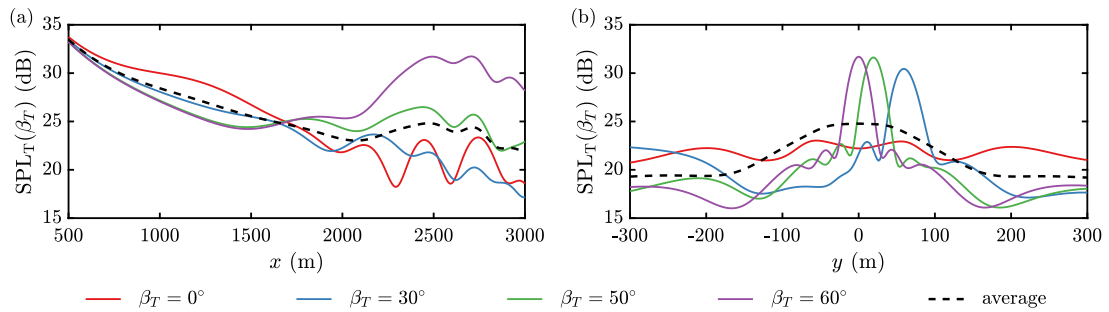
Fig. 14. Sound pressure levels $SPL_T(\beta_T)$ computed with 3DPE for the full wind turbine along the line (a) $y = 0$ and $z = 0$ and (b) $x = 2500$ m and $z = 0$ for four angular positions: (red) $\beta_T = 0°$, (blue) $\beta_T = 30°$, (green) $\beta_T = 50°$, and (purple) $\beta_T = 60°$. The dashed black line corresponds to the average SPL over one rotation.

blade ($\beta = 0°$) and the two focal zones centered around $x \approx 2000$ m and $y = \pm100$ m are due to the two blades with $\beta = 120°$ and 240°. Similarly, in the plane $x = 3000$ m, the blade with $\beta = 0°$ generates the focal zone at $y = 0$ and $z > 100$ m and the blades with $\beta = 120°$ and 240° the focal zones at $z = 100$ m and $|y| > 50$ m. As the blades rotate, the focal zones move simultaneously. On the ground, they seem to spin around $x = 1800$ m and $y = 0$. Also note that, while the blades are rotating counterclockwise, the focal zones in the plane $x = 3000$ m rotate clockwise because of horizontal refraction. (An animation showing the SPL for several rotor angles and for the three stability conditions is provided as supplementary material (movie 2).)

The motion of the focal zones with the rotation of the blades induces large variations of SPL at given positions, as illustrated in Fig. 14. Fig. 14(a) shows the SPL along the line $y = 0$ and $z = 0$ for four angular positions. For $x < 1700$ m, the highest levels are obtained for $\beta_T = 0°$. As observed in Fig. 13(a), this is due to the focal zone associated with the upwards pointing blade. For $x > 2200$ m, significant differences in the SPL are observed depending on the angular position. In particular, the SPL at $x = 2500$ m reaches 32 dB for $\beta_T = 60°$, which is comparable to the SPL at $x = 500$ m. These large SPL are obtained when one of the blades is pointing downwards, as seen in Fig. 13. The SPL is small otherwise, around 20–25 dB. The SPL along the line $x = 2500$ m and $z = 0$ is plotted in Fig. 14(b). One finds again near $y = 0$ a large amplification of the SPL in a zone with a small spatial extent, about 50–60 m, corresponding to the focal zone observed in Fig. 13 for $\beta_T = 30°$, 60°, and 90°. Also note that the SPL is almost constant for $\beta_T = 0°$ since no focal zones are observed at $x = 2500$ m for this angular position in Fig. 13(a).

4.2. Average SPL and amplitude modulation

The SPL averaged over one rotation is presented in Fig. 15. For comparison, we have plotted in Fig. 15(a) the average SPL without accounting for the wake. In this case, the average SPL shows a global decrease with distance. One can identify a slight
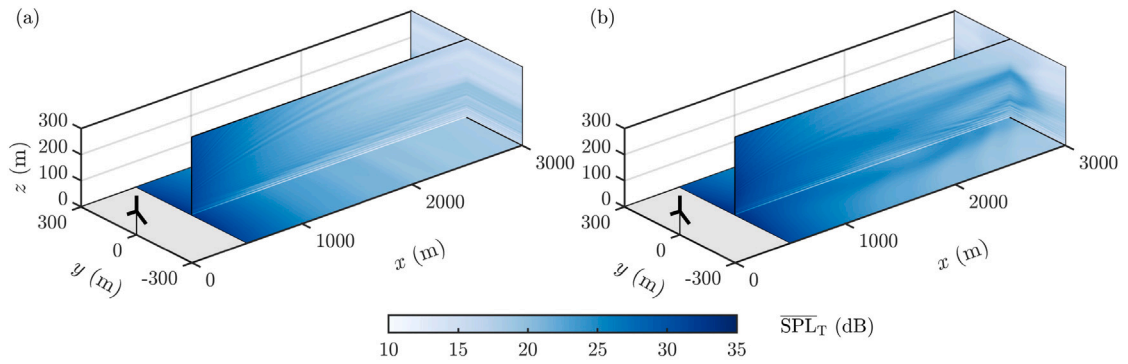
Fig. 15. Sound pressure levels averaged over one rotation in the planes $x = 3000$ m, $y = 0$, and $z = 0$ computed with 3DPE (a) without accounting for the wake and (b) with the wake.
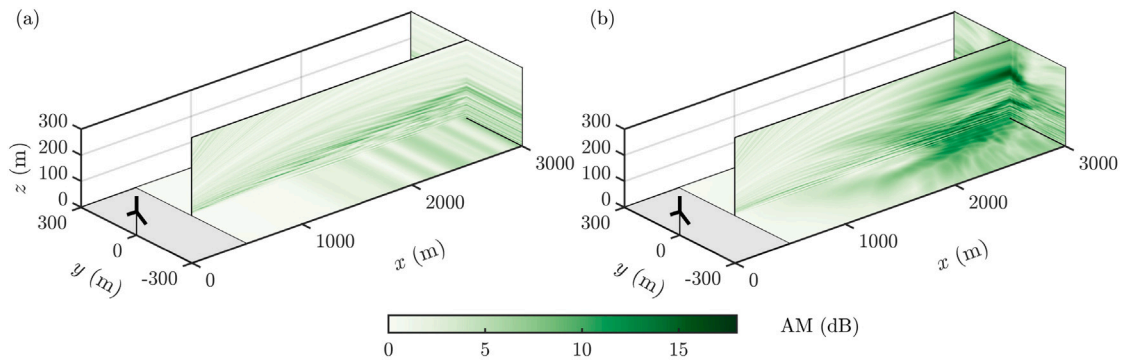
Fig. 16. Amplitude modulation in the planes $x = 3000$ m, $y = 0$, and $z = 0$ computed with 3DPE (a) without accounting for the wake and (b) with the wake.

increase in SPL in the plane $y = 0$ along a line that extends from the ground at $x = 500$ m to $z = 90$ m at $x = 3000$ m, due to refraction by the power-law wind profile. This zone of increased levels appears in plane $x = 3000$ m as an horizontal strip centered around $z = 90$ m. With the wake, in Fig. 15(b), one can observe distinct zones with increased levels on different planes. On the plane $z = 0$, SPL is amplified in a region beneath the wake along the line $y = 0$. On the plane $y = 0$, large SPL values are obtained along two curved lines, matching the focal zones observed in Fig. 8 (b) and (h) for the sources located at $y_S = 0$ and $z_S = 40$ m and $z_S = 140$ m. Finally, on the plane $x = 3000$ m, the levels are amplified along an ellipse centered around $y = 0$ and $z = 120$ m. It corresponds to the path followed by the round spot with large noise levels as the blades rotate, as observed in Fig. 13. Note the locations of zones with large levels are comparable to those reported by Heimann and Englberger [7] using a 3D ray-based sound particle model for their case labeled "18LT" (see Fig. 10 of Ref. [7]).

Maps of AM with and without accounting for the wake are plotted in Fig. 16. In both cases, AM is almost zero up to $x = 1000$ m. Without the wake, AM is large, about 10 dB, in the plane $y = 0$ around the line with increased levels noticed in Fig. 15(a). Correspondingly, this induces AM in the plane $x = 3000$ m along the line $z = 120$ m. On the ground, AM shows an oscillatory pattern, which is related to the presence of strong constructive and destructive interference due to the stable stratification when the blade is below the hub, as seen in Fig. 8(f) for a source at $z_S = 40$ m. It is partially an artifact of the harmonic computation and it would be reduced for a broadband simulation. With the wake, Fig. 16(b) presents zones with large values of AM that closely match the zones with increased average SPL noticed in Fig. 15(b). As a general rule, AM is large in focal zones. This is particularly the case if the focal zone appears for a specific angular orientation of the rotor. If so, the SPL is large for this angular orientation and reduced otherwise. Furthermore, the maximal value of AM tends to increase with distance. In the domain of interest, AM reaches 16.5 dB at $x = 3000$ m.

The evolution of the average SPL and the AM with the distance along the line $y = 0$ and $z = 0$ is shown in Fig. 17 with and without the wake. The average SPL in Fig. 17(a) without the wake reduces with distance. With the wake, the decrease in SPL is not as strong. In addition, the SPL increases by 3 dB for 2200 m $< x <$ 2800 m, which is due to the focal zone appearing for the downwards pointing blade. The AM in Fig. 17(b) without the wake shows an oscillatory pattern due to the interference reported above. For the case with the wake, AM is due to the variations in SPL as the blades rotate, as shown in Fig. 14(a). Thus, the first peak centered around $x = 1200$ m is due to the focusing originating from the upwards pointing blade. The large values for $x > 2000$ m, reaching 12 dB, are related to the focusing appearing for the downwards pointing blade.

Fig. 18 shows the evolution of the average SPL and the AM on the ground as a function of y and for several distances from the wind turbine. A slight asymmetry about the y-axis can be noticed due to the source model. Indeed, as it accounts for source motion
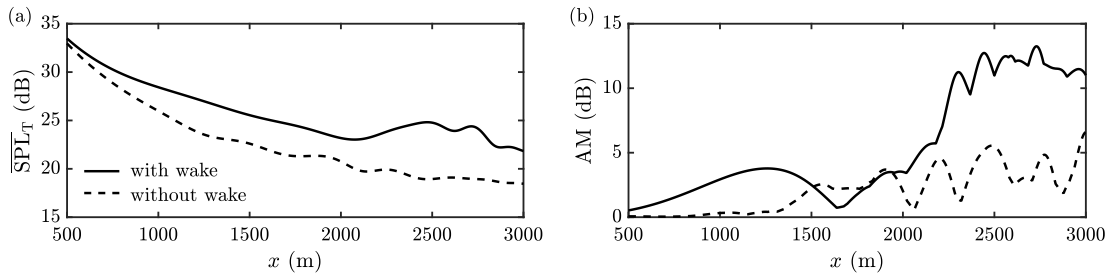
Fig. 17. Evolution of (a) the average SPL and (b) the AM along the line $y = 0$ and $z = 0$ computed with 3DPE: (solid line) with the wake and (dashed line) without the wake.
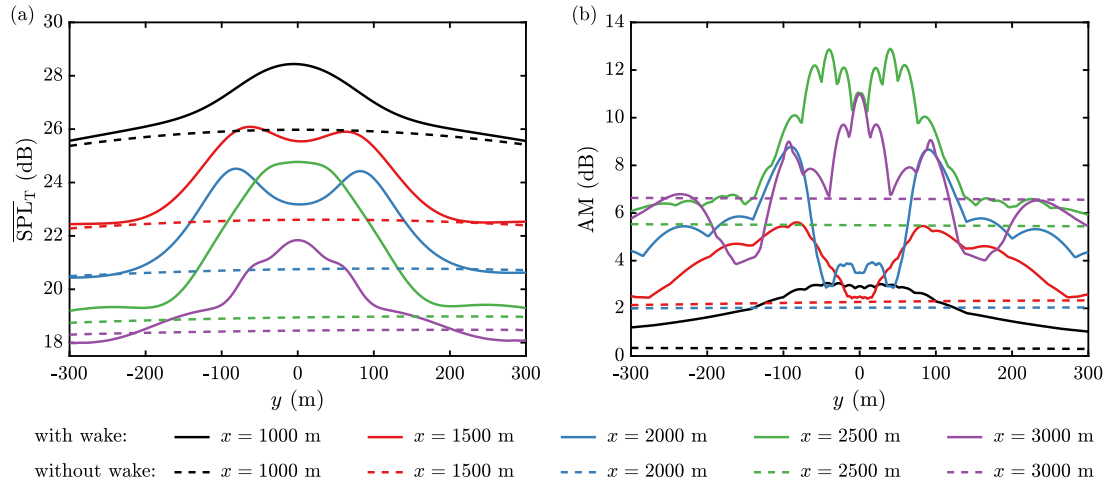
Fig. 18. Evolution of (a) the average SPL and (b) the AM along the lines $z = 0$ and (black) $x = 1000$ m, (red) $x = 1500$ m, (blue) $x = 2000$ m, (green) $x = 2500$ m, and (purple) $x = 3000$ m computed with 3DPE: (solid lines) with the wake and (dashed lines) without the wake.

effects (Doppler shift and convective amplification), the SPL depends on the blade rotation direction. In Fig. 18(a), it is observed that the effect of the wake on the average SPL is limited to $|y| < 200$ m, corresponding to twice the rotor diameter. For larger values of y, the SPL is almost equal to that without the wake. Note that the maximum of SPL for a given distance is not always obtained for $y = 0$. For x between 1500 and 2000 m, the maximum is shifted along the y-axis up to ± 100 m. In Fig. 18(b), the evolution of the AM along the y-axis depends significantly on the downstream location. Indeed, for $x = 1000$ m, AM is related to the focusing due to one of the blades pointing upwards. In this case, AM is centered around $y = 0$ and is small, below 3 dB. For $x = 1500$ and 2000 m, AM is caused by the motion of the three focal zones as the blades are rotating, as observed in Fig. 13. The curve of AM presents two bumps centered around $y = \pm 100$ m. Finally, for $x = 2500$ and 3000 m, the large values of AM result from the focal zone generated when one of the blade is pointing downwards, and AM is again centered around $y = 0$. The narrow bumps on the curves are due to the angular step of $10°$ and would be smoothed out using a smaller angular step. Note again, that, the maximal values of AM for a given downstream location are obtained in zones where the average SPL is highest.

4.3. Comparison between results for $N \times 2DPE$ and 3DPE

We now compare the results obtained with $N \times 2$DPE and 3DPE. The maps of SPL for a single blade obtained with $N \times 2$DPE are shown in Fig. 19. Comparing with 3DPE in Fig. 12, it is clear that 3D propagation effects are critical for an accurate description of focal zones. Note, however, that results with $N \times 2$DPE are in agreement with those of 3DPE outside the focal zones. As discussed in Section 3 for a single point source, the $N \times 2$DPE approach does not predict the focal zones resulting from horizontal refraction. This is especially visible in the plane $x = 3000$ m when the blade is pointing upwards ($\beta = 0°$) in Fig. 19(a) or downwards ($\beta = 180°$) in Fig. 19(c). In addition, the focal zones at the ground predicted with $N \times 2$DPE are more spread out than in 3DPE, as observed for $\beta = 90°$ in Fig. 19(b). Also, the corresponding levels near focal zones are much lower. Thus, the maximum SPL at the ground for $x > 1500$ m is 24 dB with $N \times 2$DPE, compared to 32 dB for 3DPE.

Fig. 20(a) presents the maps of average SPL determined with the $N \times 2$DPE approach. They do not show the high SPL zones captured using the 3DPE method (Fig. 15(b)). The only noticeable zone of increased SPL corresponds to an horizontal band for $z < 160$ m visible in the planes $y = 0$ and $x = 3000$ m. The AM map for $N \times 2$DPE in Fig. 20(b) is also largely different from that for
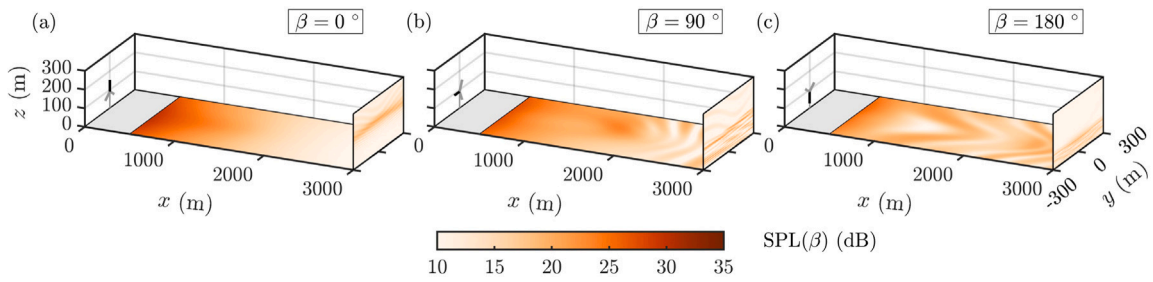
Fig. 19. Sound pressure levels SPL(β) computed with the $N \times 2$DPE approach in the planes $x = 3000$ m and $z = 0$ due to a single wind turbine blade and for three angular positions: (a) $\beta = 0°$, (b) 90°, and (c) 180°. The blade emitting sound is colored in black.
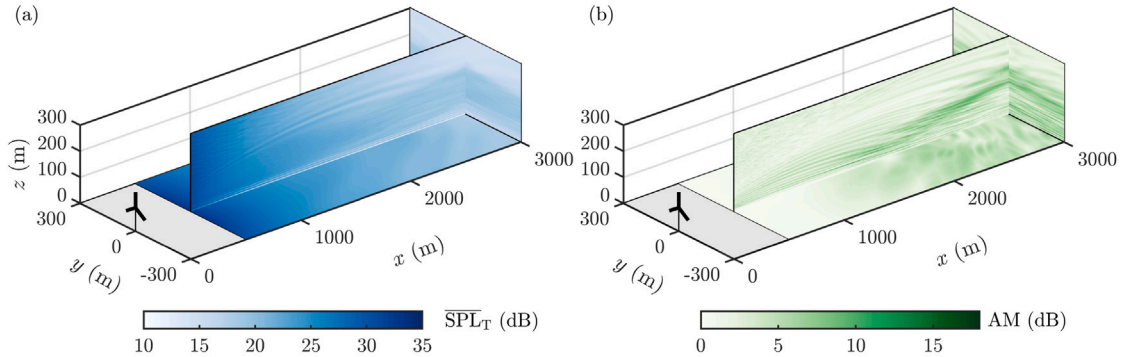
Fig. 20. (a) SPL averaged over one rotation and (b) AM in the planes $x = 3000$ m, $y = 0$, and $z = 0$ obtained with the $N \times 2$DPE approach.
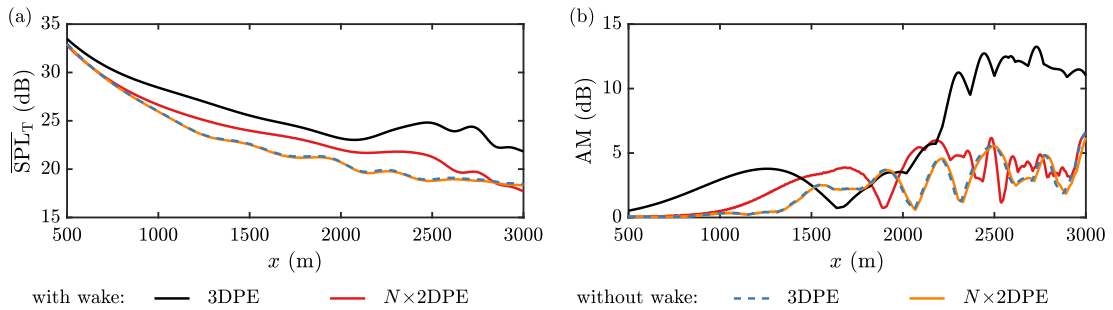
Fig. 21. Evolution of (a) the average SPL and (b) the AM along the line $y = 0$ and $z = 0$, computed with (solid black line) 3DPE and (solid red line) $N \times 2$DPE. The corresponding results obtained with 3DPE and $N \times 2$DPE without the wake are plotted in blue dashed lines and orange solid lines, respectively.

3DPE in Fig. 16(b). In the plane $y = 0$, AM is large on a curved line which corresponds approximately to the focal zone due to a source at the hub (see Fig. 8(e)). In the plane $x = 3000$ m, AM is only significant along an horizontal line centered at $z = 130$ m. On the ground, AM is zero up to $x = 1000$ m, then increases, and is rather homogeneous from $x = 2000$ m with a value around 6 dB. Overall, AM is considerably reduced with the $N \times 2$DPE, with a maximum of 12 dB compared to 16.5 dB for 3DPE.

Fig. 21 compares the evolution of the average SPL and the AM along the line $y = 0$ and $z = 0$ for $N \times 2$DPE and 3DPE. First of all, it could be checked that 3DPE and $N \times 2$DPE give similar results without the wake. In Fig. 21(a), one notes that the $N \times 2$DPE predicts an increase in SPL due to the wake. However, it is smaller than that obtained with 3DPE: the difference in the average SPL between $N \times 2$DPE and 3DPE is below 2 dB for $x < 2000$ m and reaches 4.5 dB around $x = 2700$ m. In Fig. 21(b), the AM predicted with $N \times 2$DPE for $x < 2000$ m shows an increase by 4 dB, which is comparable to that obtained with 3DPE. However, the AM peak is centered at a larger distance with $N \times 2$DPE. For $x > 2000$ m, AM is around 6 dB with $N \times 2$DPE, while it reaches 12 dB for 3DPE, because focusing due to horizontal refraction is not predicted in $N \times 2$DPE.

The evolution of the average SPL and the AM for $N \times 2$DPE and 3DPE is shown in Fig. 22 on the ground along the lines $x = 1500$ m and $x = 2500$ m. In Fig. 22(a), it is found again that $N \times 2$DPE underestimates the SPL in the downwind direction, with respect to 3DPE. It can also be noted that the increase in SPL occurs in a wider zone than with 3DPE. Concerning AM in Fig. 22(b), results with $N \times 2$DPE and 3DPE are comparable for $x = 1500$ m: we observe an increase in AM for $|y| < 250$ m with a dip centered at $y = 0$, especially noticeable for 3DPE. However, at $x = 2500$ m, the evolution of AM along the y-axis is significantly different. While
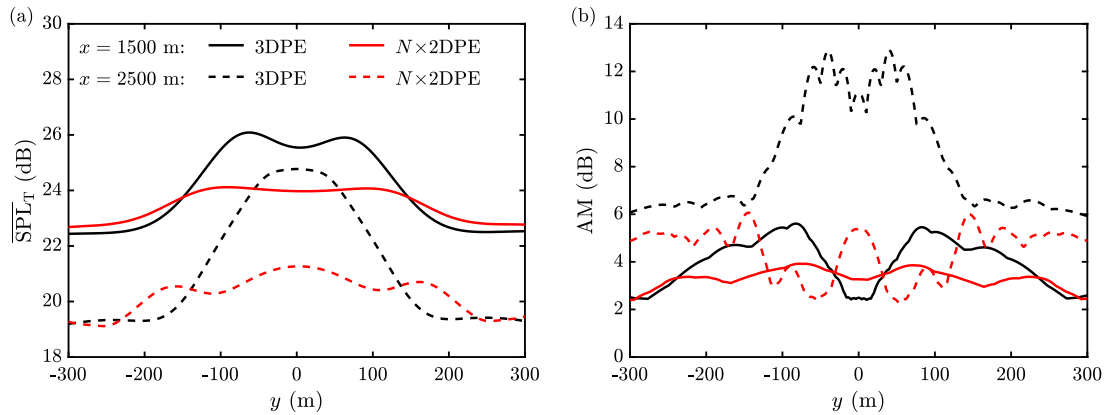
Fig. 22. Evolution of (a) the average SPL and (b) the AM along the lines $z = 0$ and (solid lines) $x = 1500$ m, and (dashed lines) $x = 2500$ m, computed with (black) 3DPE and (red) $N \times 2$DPE.

3DPE predicts a large increase of AM in the region affected by the wake ($|y| < 150$ m), $N \times 2$DPE results show a reduction of AM with respect to its value for $|y| > 150$ m except near $y = 0$.

5. Wind turbine noise propagation in neutral and unstable boundary layers

Wind turbine noise propagation for a neutral and an unstable atmosphere is now considered and the results are compared with those for the stable atmosphere. As in Section 4, the source frequency is 100 Hz. The SPL computed for a given rotor orientation ($\beta_T = 60°$) and for the three stability conditions obtained using both 3DPE and $N \times 2$DPE is shown in Fig. 23. First, let us examine the 3DPE results. For ease of comparison, the result for the stable atmosphere is again plotted in Fig. 23(a). For the neutral atmosphere in Fig. 23(b), close correspondence is found with the SPL fields for a stable atmosphere. Focusing induced by the wake is clearly noticed; the focal zones identified in Section 4.1 are found again but at a greater distance. Also, the amplification of levels at the focal zones appears to be significantly reduced. Thus, while the SPL can reach 32 dB locally for $x > 2000$ m in the stable case, it does not exceed 23 dB in the neutral case. This is even more accentuated for the unstable atmosphere in Fig. 23(c). Indeed, the SPL fields are rather homogeneous and the amplification at focal zones is hardly noticeable. As a consequence, the highest value of SPL for $x > 2000$ m is only 21 dB. Overall, sound focusing shows less importance in the neutral and unstable conditions. This is due to the combined effect of a lower velocity deficit in the wake, which tends to reduce refraction induced by the wake, and to a lower vertical shear of the ABL wind profile, which tends to move the focal zones farther to the source. Consider now the $N \times 2$DPE results. The SPL compares much more favorably with the 3DPE in the neutral case in Fig. 23(e) than in the stable case in Fig. 23(d). This is mainly due to the reduced importance of horizontal refraction, although the two focusing zones still present in the $z = 0$ plane for $x < 2000$ m with 3DPE are not visible with $N \times 2$DPE. Finally, the SPL maps for the unstable atmosphere look similar using 3DPE and $N \times 2$DPE.

The maps of the average SPL and AM are shown in Fig. 24 for the neutral atmosphere with and without the wake using 3DPE and $N \times 2$DPE. The average SPL with the wake predicted with 3DPE in Fig. 24(b) presents slightly larger values than without the wake. One can distinguish zones with amplified levels, but they are less distinct than those for the stable atmosphere in Fig. 15(b). Finally, the average SPL fields for the $N \times 2$DPE with the wake in Fig. 24(c) are between those for the 3DPE with the wake and without the wake. The AM without the wake is very similar to that for the stable atmosphere in Fig. 16(a). However, AM due to the interference pattern at the ground is largely attenuated. Accounting for the wake in the 3DPE simulations, AM is mostly noticeable for $x > 2000$ m. At ground level, the maximum is not directly beneath the turbine but on either side of it. On the $x = 3000$ m plane, AM is significant for $z < 120$ m. Note that AM is overall greatly reduced compared to the stable case, with a maximum of 7.6 dB on the ground as compared to 13.6 dB. The AM field with the $N \times 2$DPE corresponds fairly well to that of the 3DPE. On the ground, it presents an inverted V-shape pattern, that closely matches the AM field with the 3DPE.

For conciseness, the corresponding results for the unstable atmosphere are not shown. In this case, while the wake still has an effect on the acoustic field, little differences are noticed between the results for the 3DPE and the $N \times 2$DPE. In addition, the AM has small values, compared to the stable case, with a maximum around 2 dB.

The evolution of the average SPL and the AM determined with 3DPE and $N \times 2$DPE is plotted in Fig. 25 along the line $y = 0$ and $z = 0$ for the three stability cases. For the average SPL in Fig. 25(a), one observes that the largest levels are obtained for the stable case, followed by the neutral case, and then the unstable case. As already observed for the stable case, a similar evolution of the levels with distance is obtained with both the $N \times 2$DPE and 3DPE. However, the $N \times 2$DPE underestimates the levels by a maximum of 2 dB for the neutral and unstable cases. Concerning the AM in Fig. 25(b), one can note a significant reduction in the neutral and unstable cases compared to the stable case, especially for $x > 2000$ m. Indeed, the focal zone inducing the large values of AM at long range in the stable case is not present in the neutral and unstable cases. Finally, while the $N \times 2$DPE does not predict
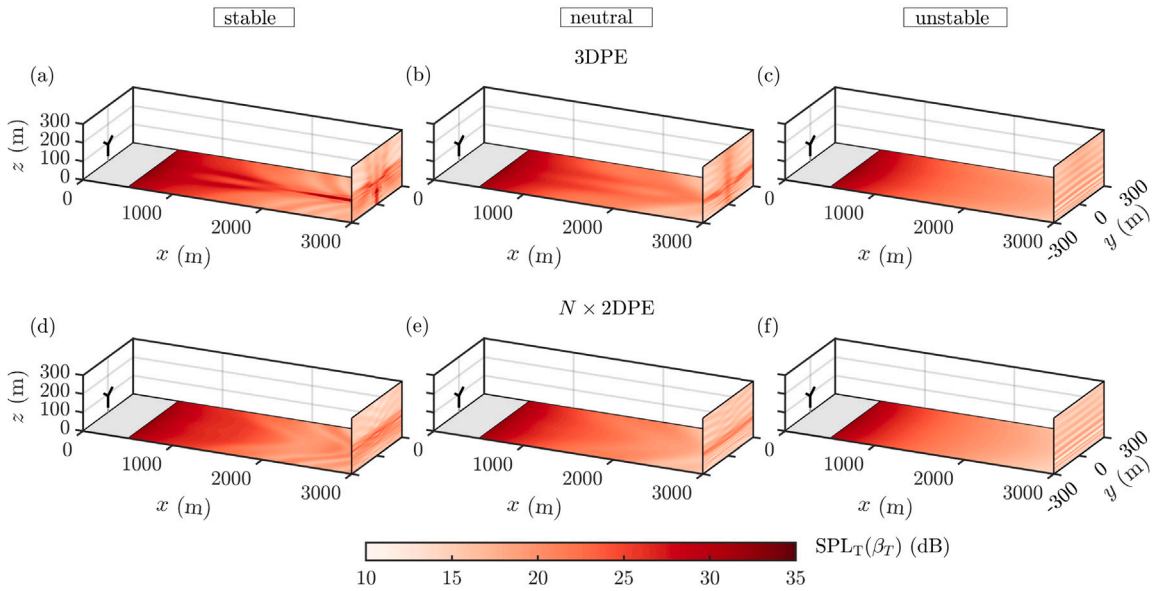
Fig. 23. Sound pressure levels $\mathrm{SPL_T}$ for the full wind turbine for $\beta_T = 60°$ computed with (a)–(c) 3DPE and (d)–(f) $N \times 2\mathrm{DPE}$ for the three stability conditions: stable in (a) and (d), neutral in (b) and (e), and unstable in (c) and (f).
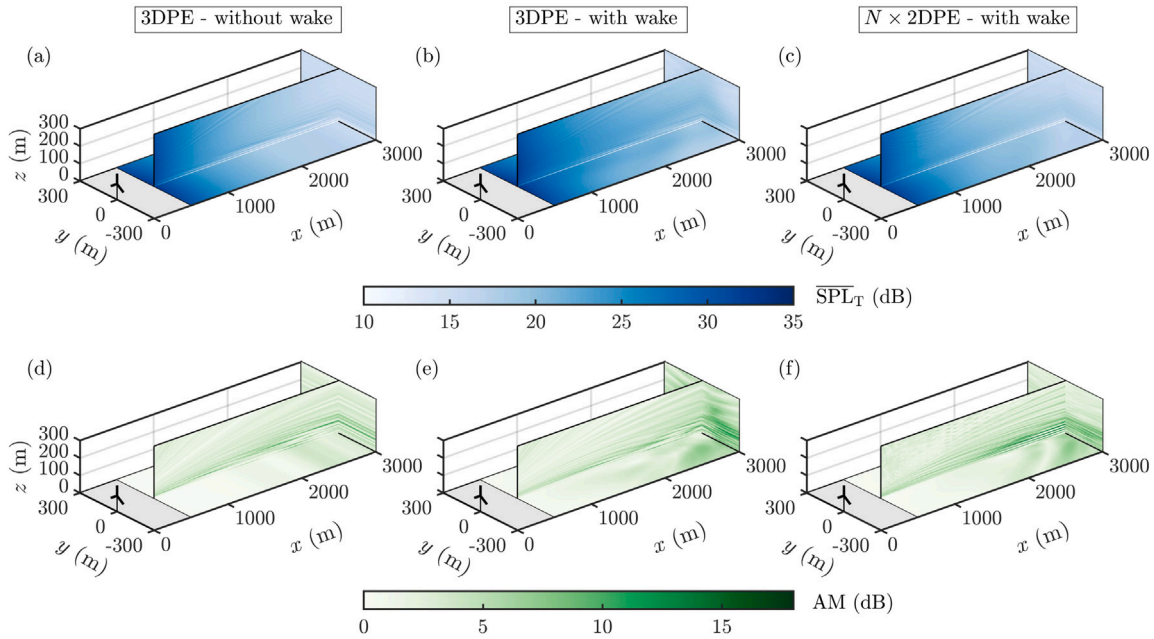
Fig. 24. Maps in the planes $x = 3000$ m, $y = 0$, and $z = 0$ of (a)–(c) the average SPL and (d)–(f) the AM for the neutral atmosphere computed with (a) and (d) 3DPE without wake, (b) and (e) 3DPE and (c) and (f) $N \times 2\mathrm{DPE}$ with wake.

the evolution of AM with distance accurately, it provides a fair estimate of the AM magnitude for the neutral and unstable cases, contrary to the stable case.

Fig. 26 shows the evolution of the average SPL and the AM along y at the ground and for $x = 2500$ m for the three stability cases. For the SPL in Fig. 26(a), the curves with 3DPE present a bump centered at $y = 0$. Compared to the value outside the wake, the largest increase is obtained for the stable case with 5.5 dB, followed by the neutral case with 3.5 dB, and the unstable case with 3 dB. The width of the bump also depends on the atmospheric stability: it is largest for the unstable atmosphere and smallest for the stable atmosphere. In contrast to the stable case, the $N \times 2\mathrm{DPE}$ predicts the correct evolution of the average SPL with y, but underestimates the maximum SPL by around 2 dB. The corresponding AM in Fig. 26(b) shows different evolution depending on
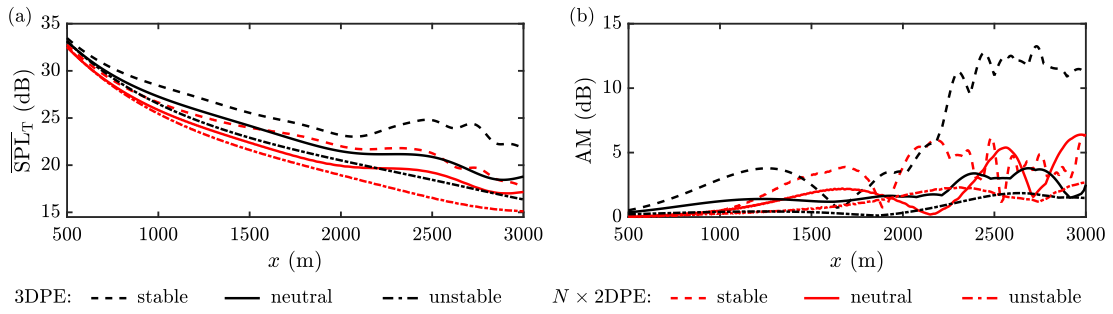
Fig. 25. Evolution of (a) the average SPL and (b) the AM along the line $y = 0$ and $z = 0$, computed with (black) 3DPE and (red) $N \times 2$DPE for the (dashed) stable, (solid) neutral, and (dash-dotted) unstable atmospheres.
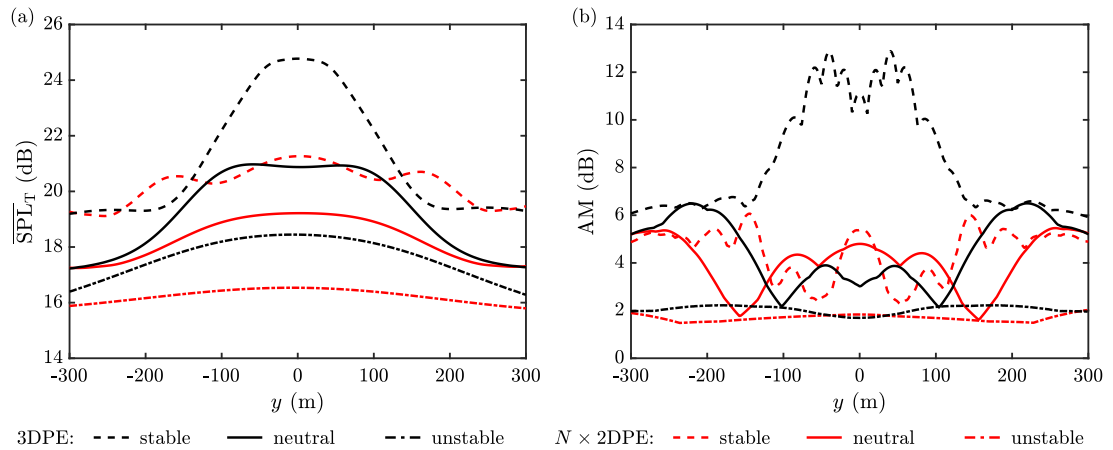
Fig. 26. Evolution of (a) the average SPL and (b) the AM along the y-axis on the ground for $x = 2500$ m, computed with (black) 3DPE and (red) $N \times 2$DPE for the (dashed) stable, (solid) neutral, and (dash-dotted) unstable atmospheres.

the stability conditions. While AM is highest near $y = 0$ in the stable case, the largest values are obtained for $y = \pm 200$ m for the neutral atmosphere. Finally, for the unstable atmosphere, AM is almost constant and the effect of the wake is negligible. Though the $N \times 2$DPE is not suitable to predict AM in the stable case, good agreement is found between $N \times 2$DPE and 3DPE for the neutral and unstable conditions.

6. Conclusion

A comprehensive study has been conducted to analyze the impact of 3D wake effects on wind turbine sound propagation. Using advanced 2D and 3D parabolic equation simulations, we examined stable, neutral, and unstable atmospheric conditions. Our findings demonstrate the substantial influence of 3D effects, particularly in stable atmospheric conditions. While the 2D approach accurately predicts focal zones due to vertical refraction, it underestimates the noise levels in these zones compared to 3D simulations. Furthermore, the 2D approach overlooks horizontal refraction, which involves bending of sound waves due to changes in wind speed and direction in the horizontal plane. The resulting caustics are therefore not accounted for either. Consequently, the 2D simulation underestimates long-range amplitude modulation.

This study focused on analyzing results for 100 Hz, but the main trends are similar in the 50–125 Hz range. Nevertheless, exploring higher frequencies in 3D simulations to determine overall sound pressure levels and associated amplitude modulation would be beneficial. While the impact of the scattering by turbulence caused by the wake was noticeable in the 2D simulations by Barlas et al. [14], further work is required to understand this in 3D simulations. Overall, this work underscores the importance of a 3D approach to refine noise prediction models and develop more effective mitigation strategies for wind turbine noise, ultimately leading to better community acceptance and integration.

CRediT authorship contribution statement

Hemant Bommidala: Writing – original draft, Investigation, Conceptualization. **Jules Colas:** Writing – review & editing, Software, Conceptualization. **Ariane Emmanuelli:** Writing – review & editing, Supervision, Conceptualization. **Didier Dragna:** Writing – review & editing, Supervision, Conceptualization. **Codor Khodr:** Supervision, Software, Conceptualization. **Benjamin Cotté:** Writing – review & editing, Software, Conceptualization. **Richard J.A.M. Stevens:** Writing – review & editing, Conceptualization.

Declaration of competing interest

Acknowledgments

Appendix A. Effect of frequency for a stable atmosphere

The largest 3D effects of the wake on wind turbine sound propagation have been reported for a stable atmosphere. Results in Section 4 have been shown for a source frequency of 100 Hz. In order to verify that the findings are not specific to this particular frequency, wind turbine sound propagation in a stable atmosphere is considered for another set of frequencies in this Appendix.

Fig. A.1 presents the maps of average SPL and AM for frequencies of 50, 75, and 125 Hz. Note that the source amplitude varies with frequency. For comparison purpose, we consider the normalized average SPL denoted $\Delta\overline{SPL}_T$ using the SPL at $x = 500$ m and $y = z = 0$ as the reference value, i.e. $\Delta\overline{SPL}_T(\mathbf{x}) = \overline{SPL}_T(\mathbf{x}) - \overline{SPL}_T(x = 500\ m,\ y = 0,\ z = 0)$. The structure of the average SPL maps in Fig. A.1(a)–(c) clearly corresponds to that for $f = 100$ Hz in Fig. 15(b). In particular, focal zones are noticed and they occur in the same locations for $f = 75$ and 125 Hz as those observed for $f = 100$ Hz. For $f = 50$ Hz, the focal zones are slightly blurred. The AM maps in Fig. A.1(d)–(f) present more variation with frequency. At the lowest frequency, i.e. $f = 50$ Hz, no specific feature can be identified. For $f = 75$ Hz, one can observe zones with large AM in the planes $y = 0$ and $x = 3000$ m corresponding to those for $f = 100$ Hz in Fig. 16(b), while AM on the ground is remarkably different. Finally, the AM maps for $f = 125$ Hz are very close to those for $f = 100$ Hz. Note that AM generally tends to increase with frequency.

Fig. A.2 shows the evolution of the normalized average SPL and the AM along the ground for $y = 0$ for the four frequencies. The variation of the average SPL in Fig. A.2(a) is similar. In particular, the zone with increased levels for 2200 m $< x <$ 2800 m
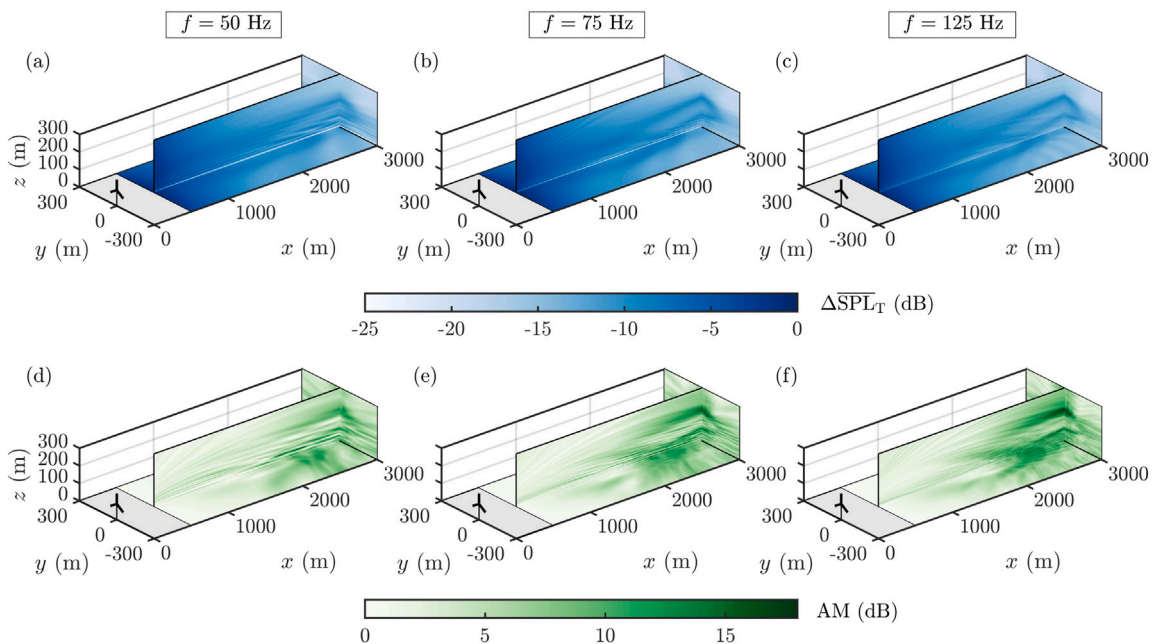
Fig. A.1. Maps in the planes $x = 3000$ m, $y = 0$, and $z = 0$ of (a)–(c) the average SPL and (d)–(f) the AM for frequencies of 50 Hz in (a) and (d), 75 Hz in (b) and (e), and 125 Hz in (c) and (f) using 3DPE. For comparison, the SPL is normalized with the reference SPL at $x = 500$ m and $y = z = 0$.
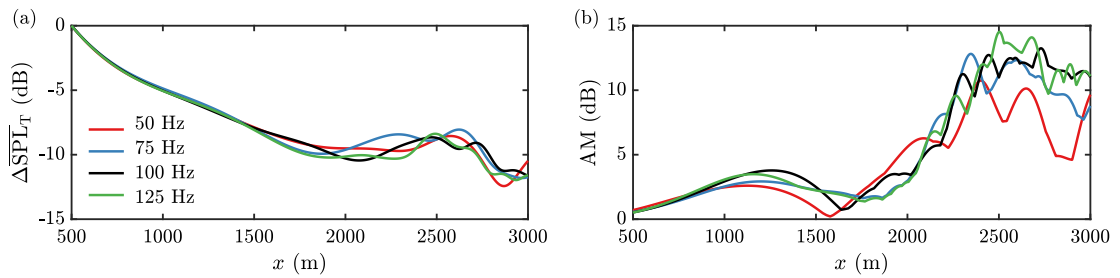
Fig. A.2. Evolution of (a) the normalized average SPL and (b) the AM along the line $y = 0$ and $z = 0$, computed with 3DPE for a frequency of (red) 50 Hz, (blue) 75 Hz, (black) 100 Hz, and (green) 125 Hz.
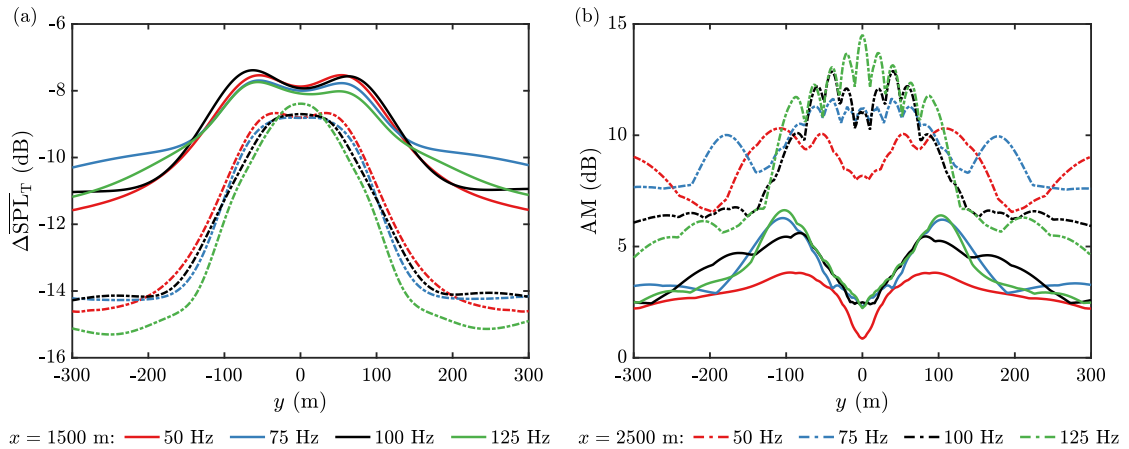
Fig. A.3. Evolution of (a) the normalized average SPL and (b) the AM along the y-axis on the ground for (solid lines) $x = 1500$ m and (dash-dotted lined) $x = 2500$ m, computed with 3DPE for a frequency of (red) 50 Hz, (blue) 75 Hz, (black) 100 Hz, and (green) 125 Hz.

is observed in all cases. The same conclusions apply to the AM in Fig. A.2(b). The bump for 1000 m $< x <$ 1700 m and the large increase for $x >$ 2000 m is found for the four curves. For the latter, AM reaches a slightly lower value for $f = 50$ Hz.

The evolution of the normalized average SPL and of the AM on the ground is plotted along the lines $x = 1500$ m and 2500 m in Fig. A.3 for the four frequencies. The average SPL in Fig. A.3(a) shows little difference. In particular, the increase in SPL due to the wake occurs in a region of the same width and the maximal value is comparable. The AM in Fig. A.3(b) presents more variation with frequency. At $x = 1500$ m, the curves for $f = 75$, 100 and 125 Hz are in close agreement, while AM for $f = 50$ Hz is lower. However, at $x = 2500$ m, AM largely depends on the frequency. For $f = 50$ Hz, AM oscillates around 9 dB, without a noticeable increase below the wake. As the frequency increases, AM tends to increase for $|y| <$ 130 m and decreases outside this zone.

Overall, we find that the average sound pressure fields for 50, 75, and 125 Hz are very similar to those for 100 Hz. The AM fields appear to be more sensitive to the source frequency. Therefore, the results presented in Section 4 are expected to be representative of wind turbine sound propagation at low frequencies.

Appendix B. Supplementary data

Supplementary material related to this article can be found online at https://doi.org/10.1016/j.jsv.2025.119036.

Data availability

Data will be made available on request.

References

[1] S. Lee, K. Kim, W. Choi, S. Lee, Annoyance caused by amplitude modulation of wind turbine noise, Noise Control Eng. J. 59 (2011) 38–46, http://dx.doi.org/10.3397/1.3531797.
[2] C. Ioannidou, S. Santurette, C.-H. Jeong, Effect of modulation depth, frequency, and intermittence on wind turbine noise annoyance, J. Acoust. Soc. Am. 139 (2016) 1241–1251, http://dx.doi.org/10.1121/1.4944570.

[3] E. Barlas, W.J. Zhu, W.Z. Shen, K.O. Dag, P. Moriarty, Consistent modelling of wind turbine noise propagation from source to receiver, J. Acoust. Soc. Am. 142 (2017) 3297–3310, http://dx.doi.org/10.1121/1.5012747.

[4] B. Cotté, Extended source models for wind turbine noise propagation, J. Acoust. Soc. Am. 145 (2019) 1363–1371, http://dx.doi.org/10.1121/1.5093307.

[5] K.L. Hansen, P.D. Nguyen, B. Zajamsek, P. Catcheside, C.H. Hansen, Prevalence of wind farm amplitude modulation at long-range residential locations, J. Sound Vib. 455 (2019) 136–149, http://dx.doi.org/10.1016/j.jsv.2019.05.008.

[6] P.D. Nguyen, K.L. Hansen, B. Lechat, C.H. Hansen, P. Catcheside, B. Zajamsek, Audibility of wind farm infrasound and amplitude modulated tonal noise at long-range locations, Appl. Acoust. 201 (2022) 109106, http://dx.doi.org/10.1016/j.apacoust.2022.109106.

[7] D. Heimann, A. Englberger, 3D-simulation of sound propagation through the wake of a wind turbine: Impact of the diurnal variability, Appl. Acoust. 141 (2018) 393–402, http://dx.doi.org/10.1016/j.apacoust.2018.06.005.

[8] D. Heimann, A. Englberger, A. Schady, Sound propagation through the wake flow of a hilltop wind turbine - A numerical study, Wind. Energy 21 (2018) 650–662, http://dx.doi.org/10.1002/we.2185.

[9] S. Lee, D. Lee, S. Honhoff, Prediction of far-field wind turbine noise propagation with parabolic equation, J. Acoust. Soc. Am. 140 (2016) 767–778, http://dx.doi.org/10.1121/1.4958996.

[10] B. Kayser, B. Cotté, D. Ecotière, B. Gauvreau, Environmental parameters sensitivity analysis for the modeling of wind turbine noise in downwind conditions, J. Acoust. Soc. Am. 148 (2020) 3623–3632, http://dx.doi.org/10.1121/10.0002872.

[11] J. Colas, A. Emmanuelli, D. Dragna, P. Blanc-Benon, B. Cotté, R.J.A.M. Stevens, Wind turbine sound propagation: Comparison of a linearized Euler equations model with parabolic equation methods, J. Acoust. Soc. Am. 154 (2023) 1413–1426, http://dx.doi.org/10.1121/10.0020834.

[12] J. Colas, A. Emmanuelli, D. Dragna, P. Blanc-Benon, B. Cotté, R.J.A.M. Stevens, Impact of a two-dimensional steep hill on wind turbine noise propagation, Wind. Energy Sci. 9 (2024) 1869–1884, http://dx.doi.org/10.5194/wes-9-1869-2024.

[13] D. Heimann, Y. Käsler, G. Gross, The wake of a wind turbine and its influence on sound propagation, Meteorol. Z. 20 (2011) 449–460, http://dx.doi.org/10.1127/0941-2948/2011/0273.

[14] E. Barlas, W.J. Zhu, W.Z. Shen, M. Kelly, S.J. Andersen, Effects of wind turbine wake on atmospheric sound propagation, Appl. Acoust. 122 (2017) 51–61, http://dx.doi.org/10.1016/j.apacoust.2017.02.010.

[15] J. Jonkman, S. Butterfield, W. Musial, G. Scott, Definition of a 5-MW Reference Wind Turbine for Offshore System Development, Technical Report NREL/TP-500-38060, NREL, Golden, CO, USA, 2009.

[16] G.P. van der Berg, Effects of the wind profile at night on wind turbine sound, J. Sound Vib. 277 (2004) 955–970, http://dx.doi.org/10.1016/j.jsv.2003.09.050.

[17] M. Bastankhah, F. Porté-Agel, A new analytical model for wind-turbine wakes, Renew. Energy 70 (2014) 116–123, http://dx.doi.org/10.1016/j.renene.2014.01.002.

[18] F. Blondel, M. Cathelain, An alternative form of the super-Gaussian wind turbine wake model, Wind. Energy Sci. 5 (2020) 1225–1236, http://dx.doi.org/10.5194/wes-5-1225-2020.

[19] M. Abkar, F. Porté-Agel, Influence of atmospheric stability on wind-turbine wakes: A large-eddy simulation study, Phys. Fluids 27 (2015) 035104, http://dx.doi.org/10.1063/1.4913695.

[20] Y. Tian, B. Cotté, Wind turbine noise modeling based on Amiet's theory: Effects of wind shear and atmospheric turbulence, Acta Acust. United Ac. 102 (2016) 626–639, http://dx.doi.org/10.3813/AAA.918979.

[21] J. Han, S.P. Arya, S. Shen, Y.-L. Lin, An Estimation of Turbulent Kinetic Energy and Energy Dissipation Rate Based on Atmospheric Boundary Layer Similarity Theory, NASA/CR- 2000-210298, 2000.

[22] S. Lee, Empirical wall-pressure spectral modeling for zero and adverse pressure gradient flows, AIAA J. 56 (2018) 1818–1829, http://dx.doi.org/10.2514/1.J056528.

[23] M. Drela, XFOIL: An analysis and design system for low Reynolds number airfoils, in: T.J. Mueller (Ed.), Low Reynolds Number Aerodynamics, in: Lecture Notes in Engineering, Vol. 54, Springer, Berlin, Heidelberg, 1989, http://dx.doi.org/10.1007/978-3-642-84010-4_1.

[24] S. Sinayoko, M. Kingan, A. Agarwal, Trailing edge noise theory for rotating blades in uniform flow, Proc. R. Soc. A 469 (2013) 20130065, http://dx.doi.org/10.1098/rspa.2013.0065.

[25] V.E. Ostashev, D.K. Wilson, Acoustics in Moving Inhomogeneous Media, second ed., CRC Press, Boca Raton, FL, USA, 2016.

[26] V.E. Ostashev, J. Colas, D. Dragna, D.K. Wilson, Phase-preserving narrow- and wide-angle parabolic equations for sound propagation in moving media, J. Acoust. Soc. Am. 155 (2024) 1086–1102, http://dx.doi.org/10.1121/10.0024460.

[27] C. Khodr, M. Azarpeyvand, D.N. Green, An iterative three-dimensional parabolic equation solver for propagation above irregular boundaries, J. Acoust. Soc. Am. 148 (2020) 1089–1100, http://dx.doi.org/10.1121/10.0001766.

[28] C. Khodr, M. Azarpeyvand, D.N. Green, Three-dimensional topographic effects on infrasound propagation across Ascension Island, Geophys. J. Int. 231 (2022) 1558–1572, http://dx.doi.org/10.1093/gji/ggac230.

[29] K. Attenborough, I. Bashir, S. Taherzadeh, Outdoor ground impedance models, J. Acoust. Soc. Am. 129 (2011) 2806–2819, http://dx.doi.org/10.1121/1.3569740.

[30] E.M. Salomons, Computational Atmospheric Acoustics, Springer, Dordrecht, Netherlands, 2001.

[31] F. Sturm, Numerical study of broadband sound pulse propagation in three-dimensional oceanic wave guides, J. Acoust. Soc. Am. 117 (2005) 1058–1079, http://dx.doi.org/10.1121/1.1855791.

[32] J.F. Scott, P. Blanc-Benon, O. Gainville, Weakly nonlinear propagation of small-wavelength, impulsive acoustic waves in a general atmosphere, Wave Motion 72 (2017) 41–61, http://dx.doi.org/10.1016/j.wavemoti.2016.12.005.